Monthly Notices of the ROYAL ASTRONOMICAL SOCIETY

MNRAS **474,** 4112–4129 (2018)
Advance Access publication 2017 November 14

doi:10.1093/mnras/stx2937

Fourteen candidate RR Lyrae star streams in the inner Galaxy

Cecilia Mateu,[1★] Justin I. Read[2] and Daisuke Kawata[3]

[1] *Centro de Investigaciones de Astronomía, AP 264, Mérida 5101–A, Venezuela*
[2] *Department of Physics, University of Surrey, Guildford GU2 7XH, UK*
[3] *Mullard Space Science Laboratory, University College London, Holmbury St Mary, Dorking, Surrey RH5 6NT, UK*

Accepted 2017 November 10. Received 2017 November 9; in original form 2017 September 22

ABSTRACT

We apply the GC3 stream-finding method to RR Lyrae stars (RRLSs) in the Catalina survey. We find 2 RRLS stream candidates at $>4\sigma$ confidence and another 12 at $>3.5\sigma$ confidence over the Galactocentric distance range $4 < D/\mathrm{kpc} < 26$. Of these, only two are associated with known globular clusters (NGC 1261 and Arp2). The remainder are candidate 'orphan' streams, consistent with the idea that globular cluster streams are most visible close to dissolution. Our detections are likely a lower bound on the total number of dissolving globulars in the inner galaxy, since many globulars have few RRLSs, while only the brightest streams are visible over the Galactic RRLS background, particularly given the current lack of kinematical information. We make all of our candidate streams publicly available and provide a new `galstreams` PYTHON library for the footprints of all known streams and overdensities in the Milky Way.

Key words: methods: data analysis – astronomical data bases: miscellaneous – stars: variables: RR Lyrae – Galaxy:halo – Galaxy: structure.

1 INTRODUCTION

In the standard Λ cold dark matter (ΛCDM) cosmological model, structures grow through the successive mergers of smaller structures (e.g. White & Rees 1978). This model gives a remarkable match to the cosmic microwave background radiation (Smoot et al. 1992; Planck Collaboration XVI 2014), the growth of large-scale structure in the Universe (e.g. Springel, Frenk & White 2006; Baur et al. 2016), and the abundance of isolated gas rich dwarf galaxies (e.g. Read et al. 2017). However, on smaller scales inside galaxies and groups there have been long-standing tensions (e.g. Bullock & Boylan-Kolchin 2017). Key amongst these is the 'missing satellites' problem (MSP). This is a discrepancy between the number of visible satellites orbiting the Milky Way (MW) and M31 and the expected number of bound dark matter haloes in ΛCDM (Klypin et al. 1999; Moore et al. 1999).

To date, understanding the origin of the MSP has focused on the *surviving* population of dwarf galaxies (e.g. Diemand, Kuhlen & Madau 2007; Lux, Read & Lake 2010; Anderhalden et al. 2013; Newton et al. 2017) and globular clusters (GCs; e.g. Moore et al. 2006). However, many dwarfs and GCs are expected to be tidally disrupted on infall to the MW, a process made more efficient by the presence of the MW stellar disc (e.g. D'Onghia et al. 2010) and by any process that can lower the central density of the MW satellites (e.g. Read et al. 2006; Peñarrubia et al. 2010). Thus, some solutions to the MSP posit a significant depletion of satellites (see e.g. the discussion in Read, Agertz & Collins 2016), while others primarily make satellites dark (e.g. Sawala et al. 2016). These lead to detectable differences, however, in the number and properties of dissolving satellites and their stellar streams (e.g. Bullock, Kravtsov & Weinberg 2001).

The above motivates building a complete census of stellar streams in the Galaxy. Such streams can also be used to directly probe the mass distribution and shape of the MW dark matter halo (e.g. Ibata et al. 2001a; Johnston, Law & Majewski 2005; Eyre & Binney 2009; Koposov, Rix & Hogg 2010; Varghese, Ibata & Lewis 2011; Lux et al. 2013; Küpper et al. 2015), to test alternative gravity models (e.g. Read & Moore 2005; Thomas et al. 2017), to hunt for ghostly dark matter 'mini-haloes' (e.g. Johnston, Spergel & Haydn 2002; Ibata et al. 2002; Carlberg 2012; Erkal, Koposov & Belokurov 2017), and – for GC streams – to constrain GC formation and evolution models (e.g. Balbinot & Gieles 2017).

With the advent of large surveys like the Sloan Digital Sky Survey, PanSTARRS and the Dark Energy Survey, the number of known stellar streams in the MW has grown dramatically (e.g. Belokurov et al. 2006b; Grillmair 2014; Torrealba et al. 2015; Balbinot et al. 2016a; Bernard et al. 2016; Li et al. 2016; Grillmair & Carlin 2016). Yet, due to incomplete sky coverage, crowding in the Galactic Centre, and dust obscuration, the full census of GC and dwarf streams remains far from complete. In this paper, we apply the 'GC3' stream-finding method (Lynden-Bell & Lynden-Bell 1995; Johnston, Hernquist & Bolte 1996; Mateu et al. 2011) to RR Lyrae stars (RRLSs) in the Catalina Sky Survey (CSS; Drake et al. 2013a,b; Torrealba et al. 2015) to hunt for stellar streams. RRLSs are well-known standard candles for which precise distances

★ E-mail: cmateu@cida.gob.ve, cecilia.mateu@gmail.com

© 2017 The Author(s)
Published by Oxford University Press on behalf of the Royal Astronomical Society

Downloaded from https://academic.oup.com/mnras/article-abstract/474/3/4112/4628071
by University College London user
on 06 March 2018

can be estimated with errors of order ∼5 per cent out to a distance beyond $D \sim 100$ kpc, or even down to ∼2 per cent when metallicity information and infrared data are available (Neeley et al. 2017; Sesar et al. 2017). They are also present in all known dwarf galaxies (Vivas & Zinn 2006; Mateu et al. 2009), many GCs (Clement et al. 2001), as well as in all Galactic components except the thin disc (Martin & Morrison 1998), which keeps foreground contamination relatively low at low Galactic latitude compared to other tracers. These properties allow us to detect even relatively faint streams (with just a dozen RRLSs of type *ab*, corresponding to a typical luminosity for a GC stream of few $\times\ 10^4 L_\odot$), even towards the Galactic Centre ($D > 4$ kpc). Due to crowding, this region has been relatively unexplored to date, yet it is where most surviving GCs are found in the MW today (e.g. Brodie & Strader 2006). As such, we may expect to find many GC streams over the region $4 < D/\mathrm{kpc} < 26$ that we are sensitive to (Section 3.2).

This paper is organized as follows. In Section 2, we present the survey data and describe our analysis pipeline. In Section 3, we describe the GC3 method used to search for tidal streams in the context of the larger *xGC3* family of great-circle cell methods. In Section 4, we present the candidate tidal streams found and summarize their properties. In Section 5, we discuss our stream candidates in comparison with known streams, clouds, and GCs in the MW, and in Section 6, we contrast our findings with predictions for GC tidal tails.

2 THE CATALINA+HSOY RR*ab* CATALOGUE

We made a compilation of the RRLSs of type *ab* from the CSS in the Northern hemisphere ferom (Drake et al. 2013a,b) and its Southern hemisphere extension, the Siding Springs Survey (SSS) from Torrealba et al. (2015). The joint CSS+SSS comprises >20 000 RR*ab* stars, covering >34 000 deg^2 in the magnitude range $14 < V < 20$ across the whole sky, except an avoidance zone at low galactic latitude $|b| \leq 15^\circ$ (Drake et al. 2013a,b; Torrealba et al. 2015).

The CSS+SSS RR*ab* catalogue constitutes a deep, clean and homogeneous sample, with consistent distances computed following the same methods in the northern and southern parts of the survey. The CSS and SSS surveys have an average completeness of 70 per cent and are fairly uncontaminated, as they focus on RRLSs of type *ab*, easy to discriminate against other types of variables with their well-sampled light curves.

In the SSS catalogue, Torrealba et al. (2015) report photometric metallicities derived following Jurcsik & Kovacs (1996) for their 10 540 RR*ab* stars. In the CSS catalogue, Drake et al. (2013a) report spectroscopic SDSS metallicities for 1416 RR*ab* stars. For the remaining stars, we used the publicly available CSS time series data[1] to compute photometric metallicities using the TFF code from Kovacs & Kupi (2007) to perform the Fourier light-curve decomposition and compute ϕ_{31}. We used equation (7) from Torrealba et al. (2015) to obtain [Fe/H] which, as in Mateu et al. (2012), we report only for stars with $D_m > 3$. The resulting combined CSS+SSS catalogue contains 21 920 RR*ab* stars.

We also matched the combined CSS+SSS RR*ab* catalogue with the Hot Stuff for One Year (HSOY) catalogue from Altmann et al. (2017) to obtain supplementary proper motion information. HSOY is a proper motion catalogue compiled using PPMXL (Roeser, Demleitner & Schilbach 2010) and *Gaia* DR1 (Gaia Collaboration et al. 2016a,b) as first and second epoch catalogues, respectively, and contains a total of ∼500 million stars down to $G = 20$. A total of 20 610 matches were found, out of which 2 665 stars (12 per cent) have relative proper motion errors smaller than 30 per cent at a median distance of ∼13 kpc. The Catalina+HSOY RR*ab* catalogue, including the photometric metallicities computed here for CSS stars, is publicly available here.[2]

2.1 Removing stars around known GCs

Stars in the main body of known GCs and dwarf galaxies will produce a strong great circle signature in the pole count maps (PCMs) when kinematic data are unavailable or scarce. To avoid these contaminating signatures, we flag and discard from our analysis all RRLSs that fulfil these two criteria: (i) lie within the angular tidal radius r_t of each GC and (ii) lie within an interval $[R_{\mathrm{min}}, R_{\mathrm{max}}]$ in heliocentric distance R_{hel} around the cluster.

For the first criterion, we compute the angular tidal radius as $r_t = r_c 10^c$ (Navin, Martell & Zucker 2016), where the concentration c and (angular) core radius r_c are taken from the GC compilation of Harris (1996) (in its 2010 edition). For dwarf galaxies, we remove stars within 10 times the half-light radius of each galaxy, taken from the compilation of McConnachie (2012).

For the second criterion, in principle, simply we should have been able to remove the stars in the volume within the selected physical threshold radius. However, when looking at the heliocentric distance distribution of RRLSs around a few known GCs, a large number of the RRLSs – within the tidal radius – appear to be much closer than the nominal distance of the cluster. For example, for M3 that is located at 10 kpc (Harris 1996), RRLSs are found down to ∼9 kpc, clearly beyond its tidal radius of ∼85 pc.

This suggests a problem with the absolute magnitude M_V assumed to compute the RRLS distances, since the distribution appears more extended only in heliocentric distance. This is most likely due to the presence of overluminous RRLSs, noted by several authors in their GC studies (e.g. Cacciari, Corwin & Carney 2005; VandenBerg, Denissenkov & Catelan 2016). Cacciari et al. (2005) proposes these are RRLSs that have evolved off the Zero Age Horizontal Branch (ZAHB). These overluminous RRLSs are observed to be ∼0.2–0.25 mag brighter (see e.g. VandenBerg et al. 2016), meaning their R_{hel} can be underestimated by as much as ∼10 per cent, consistent with what we see in the R_{hel} distribution of M3 RRLS in CSS.

This illustrates the need for using a distance scale that deals with post-ZAHB evolution that, for field RRLS, is a highly non-trivial issue. A proper treatment of this is beyond the scope of this paper, so for our purposes we assume maximum offsets of −0.3 and +0.05 mag due to post-ZAHB evolution and photometric errors, respectively, and remove stars in the interval $[mM - 0.3, mM + 0.05]$ mag, where mM corresponds to the cluster's distance modulus. For future works, however, a possible route has been suggested by Kunder, Chaboyer & Layden (2010), who, in an Oosterhoff analysis of the absolute magnitude of bulge RRLS, propose using an M_V-period-shift relation instead of the traditionally used M_V-metallicity. This may offer a way to properly estimate the absolute magnitude of these overluminous RRLSs, as Cacciari et al.'s findings support a connection between the Oosterhoff dichotomy – and hence, the period shift – and post-ZAHB evolution.

[1] Available at http://nesssi.cacr.caltech.edu/DataRelease/RRL.html.

[2] https://cmateu.github.io/Cecilia_Mateu_WebPage/CatalinaGC3_Streams.html

Downloaded from https://academic.oup.com/mnras/article-abstract/474/3/4112/4628071
by University College London user
on 06 March 2018

3 THE STREAM SEARCH

3.1 The *xGC3* family

The *xGC3* family encompasses a suite of methods to search for tidal streams by looking for overdensities in great circle bands in the sky, as seen from the Galactic Centre, an idea introduced originally by Lynden-Bell & Lynden-Bell (1995) and Johnston et al. (1996) and expanded in Mateu et al. (2011). The different methods in the family are defined by their use of the different layers of information available:

(i) *GC3* (3D): 3D position
(ii) *nGC3* (5D): 3D position + proper motions
(iii) *mGC3* (6D): 3D position + 3D velocity

Briefly, the *xGC3* methods in general consist in counting, as seen from the Galactic Centre, how many stars lie along each great circle and, in the case of *nGC3* and *mGC3* , counting how many of these also have their velocity vectors along that great circle. Labelling each great circle by its normal vector or 'pole' and going over all possible poles in the celestial sphere, a PCM is produced that displays the number of stars associated with each pole. A tidal tail will show up as a maximum or localized peak in an *xGC3* PCM, whereas a completely bound cluster or galaxy (i.e. a localized clump of co-moving stars) will show up either as a great circle in a *GC3* PCM, or as a localized peak in an *nGC3* /*mGC3* PCM thanks to the addition of kinematic information. For various examples of the PCM signatures produced by different stellar structures and the effects of observational errors in them, we refer the reader to Mateu et al. (2017; their fig. 3 and section 5.2), Mateu (2017) and for a detailed explanation of each of the methods in the family, we refer to Mateu et al. (2011) (*GC3* , *mGC3*) and Abedi et al. (2014) (*nGC3*).

The *xGC3* methods offer several advantages in the search for tidal streams: (i) they are based in the simple principle that tidal streams are approximately planar if produced in a potential that is approximately symmetric, and no knowledge or assumption of the underlying potential is required; (ii) even though in theory the methods work best for streams produced in symmetric static potentials, Mateu et al. (2017) have shown streams produced in realistic cosmologically evolving potentials can be recovered with *nGC3* ; (iii) in a PCM a tidal stream, however, its complicated distribution in radius might produces a peak that can simply be more or less stretched or deformed depending on the effect of precession and of the observational errors (see figs 3 and 4 in Mateu et al. 2017); (iv) the *xGC3* methods are implemented directly in terms observable quantities (see Mateu et al. 2011) in a way that minimizes error propagation, in particular, when using the parallax by avoiding the computation of its reciprocal; (v) the *xGC3* methods are linear; hence, depending on the information available for different stars, PCMs can be produced with the different methods and later combined into a single composite PCM by simple addition.

3.2 Computation of PCMs and peak detection

The Catalina+HSOY RRLS catalogue produced contains HSOY proper motions; however, for the majority of the RRLS, the relative errors are quite large as mentioned in Section 2. In what follows, we take as acceptable proper motions those with relative errors < 30 per cent and combine *nGC3* PCMs for those stars (2665) with *GC3* PCMs for the rest (19 255). Although these stars are few, the use of their kinematic information can help reduce foreground contamination in the combined *GC3* +*nGC3* PCM.

To compute the *GC3* and *nGC3* PCMs, we use the PYMGC3 toolkit, a PYTHON implementation of the *xGC3* methods publicly available at this GitHub repository (Mateu 2014). The *GC3* +*nGC3* PCMs were computed with a great circle tolerance of 1° (both in position and velocity) and in Galactocentric bins 1 kpc wide with offsets of 0.5 kpc to cover the full range of Galactocentric distance from 4 to 25 kpc. We assume a reference system with the Sun is located at $X = -8.5$ kpc. The grid spacing used was $0\overset{\circ}{.}5$; therefore, our PCMs have in total 82,958 pixels, out of which half are independent.

The first step before peak detection is to produce unsharp-masked PCMs, as described in detail in Section 6.2 of Mateu et al. (2017). For this, the smooth background of each PCM is estimated with a median filter by computing a pixel-by-pixel estimate of the median in a 20° radius, i.e. in a neighbourhood much larger than the features we want to identify. The smooth background is subtracted from the PCM resulting in an unsharp-masked PCM, in which sharp features are highlighted. This unsharp-masked PCM is expressed in $N\sigma$ units dividing it pixel-by-pixel by the typical standard deviation. In Mateu et al. (2017), the pixel-by-pixel standard deviation was computed as the square root of the smoothed PCM, assuming pole counts follow a Poissonian distribution. We have improved this procedure by now computing the standard deviation of the smoothed counts in an annulus around each pixel, with an inner radius equal to the size of the box used for the median estimate and an annulus width of 5°. This allows for a much better estimation of the significance of pixel counts, especially near areas with a sharply varying background which, as in this case, can appear when the input catalogue has a sharply defined avoidance zone.

The detection of peaks is made in the unsharp-masked *GC3* +*nGC3* PCMs, using the Fellwalker[3] algorithm from Berry (2015) (see Mateu et al. 2017, for a detailed description). The peak detections were made in the combined *GC3* +*nGC3* PCMs with a tolerance of 1°.

To search for GC tidal streams, one would ideally use a smaller tolerance, around $0\overset{\circ}{.}25$ to $0\overset{\circ}{.}5$ (see e.g. Ibata et al. 2001b), as these are dynamically colder than dwarf galaxy streams. However, we have chosen to perform overall detections on PCMs with a larger tolerance to reduce random noise in the PCMs, as there are relatively few RRLSs per Galactocentric distance bin (∼700–1000 stars per 1 kpc bin up to ∼25 kpc). In the next section, Table 1 summarizes all detected stream candidates.

4 STREAM CANDIDATES

The geometric and detection properties of the stream candidates are summarized in Table 1.

Table 1 indicates, for each stream candidate, an ID, the pole's Galactocentric and heliocentric coordinates (ϕ, θ) and (l, b), respectively, and the minimum and maximum heliocentric distance spanned by the candidates RRLSs. The 'central' galactic coordinates ($l_\bigcirc$, $b_\bigcirc$) mean Galactocentric distance and standard deviation, and Galactocentric stream width $\Delta\theta$ (perpendicular to the stream's plane) reported correspond to those of the densest part of each stream candidate. This was found by computing the mode of a Gaussian kernel density estimation (KDE) in the azimuth distribution along the stream's plane, after subtracting the KDE for background stars in neighbouring poles selected in an annulus around

[3] FellWalker is publicly available as part of the Starlink Software Distribution at http://starlink.eao.hawaii.edu/starlink.

Downloaded from https://academic.oup.com/mnras/article-abstract/474/3/4112/4628071
by University College London user
on 06 March 2018

Table 1. Detection and geometric properties of the stream candidates detected in *GC3 +nGC3* PCMs.

ID	Pole (ϕ, θ) (°)	Pole (l, b) (°)	R_{gal} (kpc) Mean	St. dev.	($l_\bigcirc$, $b_\bigcirc$) (°)	R_{hel} (kpc) Min	Max	$\Delta\Theta$ (°)	(pc)	Nσ-Significance 1°(0°.5)	Bts	Comment
					High-confidence candidates							
11.0-1	(104.5, 32.46)	(115.80, 43.50)	11.05	0.33	(288.98, 46.21)	6.35	12.89	1.63	313	5.1(4.7)	4.3	Corvus
20.0-1	(56.38, 46.98)	(55.26, 56.50)	20.43	0.26	(7.75, −23.94)	13.25	28.35	1.8	641	5.2(5.1)	4.7	Arp2/PS1-C
					Tentative candidates							
04.5-1	(196.08, 42.64)	(48.94, 32.00)	5.38	0.31	(328.83, −20.9)	6.0	8.78	1.68	158	4.9(5.2)	3.5	
08.0-1	(38.31, 17.41)	(59.46, 34.50)	8.64	0.26	(352.46, −29.64)	6.85	15.42	1.9	286	4.7(6.2)	3.7	
08.0-2	(106.51, 1.59)	(95.50, 0.00)	8.96	0.3	(4.45, −39.97)	2.6	13.78	1.45	226	4.4(5.3)	3.5	
09.0-1	(42.99, 33.73)	(56.87, 6.50)	9.78	0.31	(322.69, 26.85)	5.91	16.77	1.94	330	5.0(4.8)	3.8	
15.0-1	(359.05, 36.6)	(22.72, 14.50)	15.54	0.34	(286.6, 21.15)	12.8	21.72	1.88	511	4.6	3.3	
17.0-1	(135.58, 18.42)	(309.51, 0.50)	17.29	0.28	(261.26, 19.67)	12.52	21.46	1.83	552	4.4(5.6)	3.9	not-Pal5
17.5-2	(225.46, 23.67)	(209.89, 3.50)	18.05	0.2	(75.32, 42.76)	12.5	18.15	1.87	590	4.7	3.5	Hermus?
17.5-3	(220.72, 48.79)	(221.17, 29.50)	18.01	0.26	(251.24, −55.26)	11.41	22.25	1.18	371	4.2(6.5)	3.5	NGC1261?
22.0-1	(9.23, 25.58)	(357.09, 41.00)	22.06	0.3	(285.28, 38.03)	19.76	27.57	1.81	696	4.3(5.5)	3.6	
23.5-1	(257.8, 41.11)	(258.43, 43.00)	23.91	0.19	(66.24, 45.15)	15.34	26.05	1.46	611	4.8(6.7)	3.9	Hyllus?
23.5-2	(46.77, 25.44)	(44.12, 37.50)	24.18	0.31	(14.69, −48.64)	24.07	29.02	1.69	712	4.4	3.2	
24.5-1	(348.31, 15.17)	(2.00, 0.00)	24.94	0.3	(272.77, 28.92)	23.29	29.43	1.69	734	4.9	3.4	
					Possible artefacts							
04.5-2	(38.02, 29.35)	(240.09, 23.00)	4.95	0.23	(337.72, 16.98)	8.0	11.82	1.74	150	4.4	3.0	
07.0-1	(94.86, 40.23)	(90.08, 40.50)	7.61	0.29	(335.65, 26.65)	1.19	14.31	1.96	260	4.7	3.2	
07.0-2	(347.69, 4.56)	(210.49, 34.00)	7.34	0.26	(334.57, 38.45)	9.82	12.38	1.72	220	4.4(5.1)	3.7	not-Pal11?
18.5-1	(30.19, 0.51)	(192.93, 17.50)	19.16	0.26	(86.49, 41.98)	16.83	24.2	1.64	550	4.2	3.2	
20.5-3	(125.68, 7.61)	(128.35, 22.00)	21.01	0.25	(23.65, −62.65)	14.69	25.47	1.89	692	4.2	3.2	
21.5-1	(356.09, 2.25)	(338.56, 14.00)	21.74	0.25	(35.71, −59.58)	22.43	24.67	1.84	700	4.5	3.1	
25.0-1	(23.41, 22.93)	(31.23, 7.00)	25.23	0.24	(280.83, 69.63)	23.2	31.18	1.7	749	4.7	3.5	
25.0-2	(137.18, 14.05)	(154.84, 20.00)	25.5	0.22	(259.98, 38.09)	20.56	29.81	1.76	782	4.3	3.4	
					Repeated detections							
17.5-1	(128.97, 11.14)	(150.48, 23.50)	17.76	0.29	(285.04, 57.96)	12.2	18.72	1.81	561	5.3	3.6	same as 17.0-1
19.5-1	(63.96, 45.02)	(65.10, 35.50)	20.27	0.27	(8.42, −22.76)	12.1	27.8	1.75	619	4.5(5.3)	4.6	same as 20.0-1
20.5-2	(71.06, 37.03)	(81.22, 32.50)	21.1	0.23	(7.46, −24.16)	27.79	28.89	1.71	631	4.4(5.4)	3.7	same as 20.0-1
23.0-1	(227.9, 29.72)	(183.47, 22.50)	23.33	0.32	(67.03, 46.51)	16.88	25.52	1.75	713	5.0	3.3	same as 23.5-1
					Unambiguous detections of known streams							
19.5-2	(95.94, 9.9)	(95.52, 6.00)	20.43	0.25	(8.46, −24.26)	11.65	27.87	1.86	663	4.2(4.6)	3.7	Sgr
20.0-2	(88.89, 17.96)	(89.65, 17.50)	20.74	0.26	(7.93, −24.91)	12.17	28.47	1.84	667	4.7(5.2)	4.2	Sgr
20.5-1	(86.8, 19.4)	(88.58, 18.50)	20.95	0.3	(4.85, −19.2)	12.54	29.22	1.83	668	4.7(5.6)	4.4	Sgr

the pole detection[4] and renormalized to match the total number of stars in each detection. The detection significance is reported in $N\sigma$ units and indicated in parenthesis is the detection significance for those poles with a counterpart detection in the *GC3 +nGC3* PCM with a 0°.5 tolerance. The average bootstrap significance (Bts) (see following subsection) is also reported. The last column indicates whether the candidate might be associated with a known GC, based on the PCMs shown in Fig. 1 and discussed in Section 4.2.

4.1 Candidate classification: bootstrap and artefact tests

The sparsity of the RRLS sample in each radial bin, combined with the catalogue's avoidance zone ($|b| \geq 20°$), might lead to significant stochastic noise and the presence of artefacts due to abrupt changes in the PCM background caused by the catalogue edges. These effects are mitigated by the unsharp masking and by the new procedure to estimate the standard deviation locally (Section 3.2), but it is reasonable to expect them not to be completely eliminated.

[4] The annulus used was the same as for the computation of the smoothed PCM standard deviation (see Section 3.2).

To obtain a more robust estimate of the detection significance, we performed bootstrap tests: 100 bootstrap realizations of the RRLS catalogue were produced and the corresponding unsharp-masked *GC3 +nGC3* PCMs computed in $N\sigma$ units (as in Section 3.2) in the same radial bins 1 kpc wide. For each of our initial candidates, we find the maximum pole counts within 2° of the candidate's pole and store it for each bootstrapped catalogue. Finally, we compute the bootstrapped mean detection significance that is summarized in column Bts-Av in Table 1.

A high mean significance in the bootstrap tests supports the robustness of a detection against stochastic fluctuations. The bootstrap test results show two of our initial candidates have a mean significance $>4\sigma$: 11.0-1 and 20.0-1, we consider these as our *high-confidence* candidates. Two more detections are just below the 4σ threshold, 17.0-1 and 23.5-1, which have 3.9σ, but the remaining ones – a clear majority – have lower mean significance closer to $\sim 3.5\sigma$, which means overall our initial significance estimates are slightly overestimated. We classify the candidates with bootstrap mean significance $<4\sigma$ as *tentative* candidates if they pass the artefact test described below.

To check whether a given detection is a likely artefact caused by possible edge-effects of the survey in the PCMs, we create a

Downloaded from https://academic.oup.com/mnras/article-abstract/474/3/4112/4628071
by University College London user
on 06 March 2018

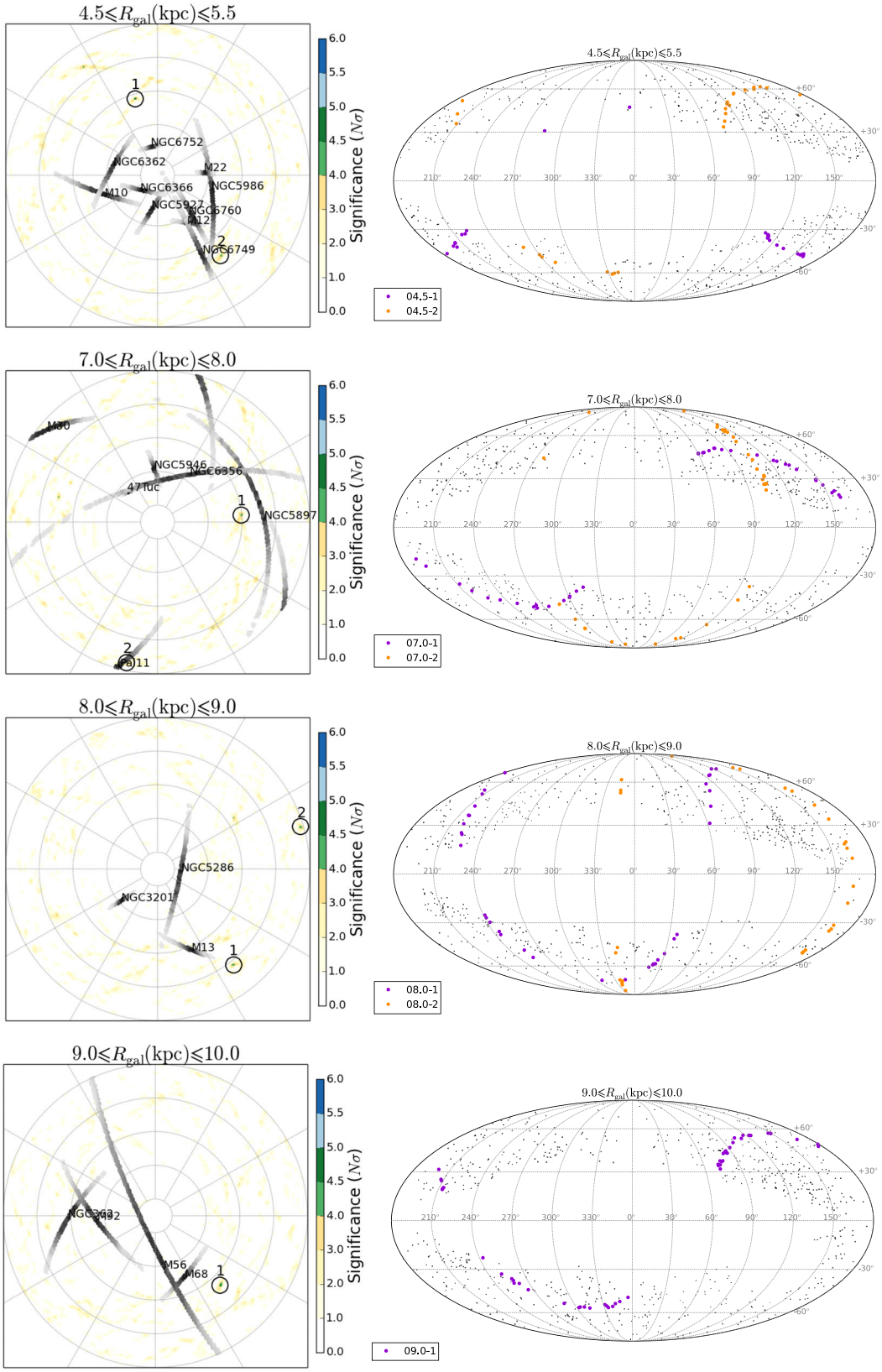

Figure 1. Left: Combined unsharp-masked *GC3 +nGC3* PCMs. The colour scale is proportional to the detection significance in $N\sigma$ units and significant detections ($>4\sigma$) are labelled and marked with an empty circle. The PCM signatures from known GCs and dwarf galaxies in each distance bin is shown as grey-scale, representing the probability density within 3σ of each cluster's proper motion errors. Right: Mollweide projection map in *Galactocentric* coordinates. The black dots indicate all the CSS+HSOY RRLSs in the given Galactocentric distance bin, the coloured dots represent the RRLSs associated with the detections made in the corresponding *GC3 +nGC3* PCM as indicated in each map's legend.

Downloaded from https://academic.oup.com/mnras/article-abstract/474/3/4112/4628071
by University College London user
on 06 March 2018

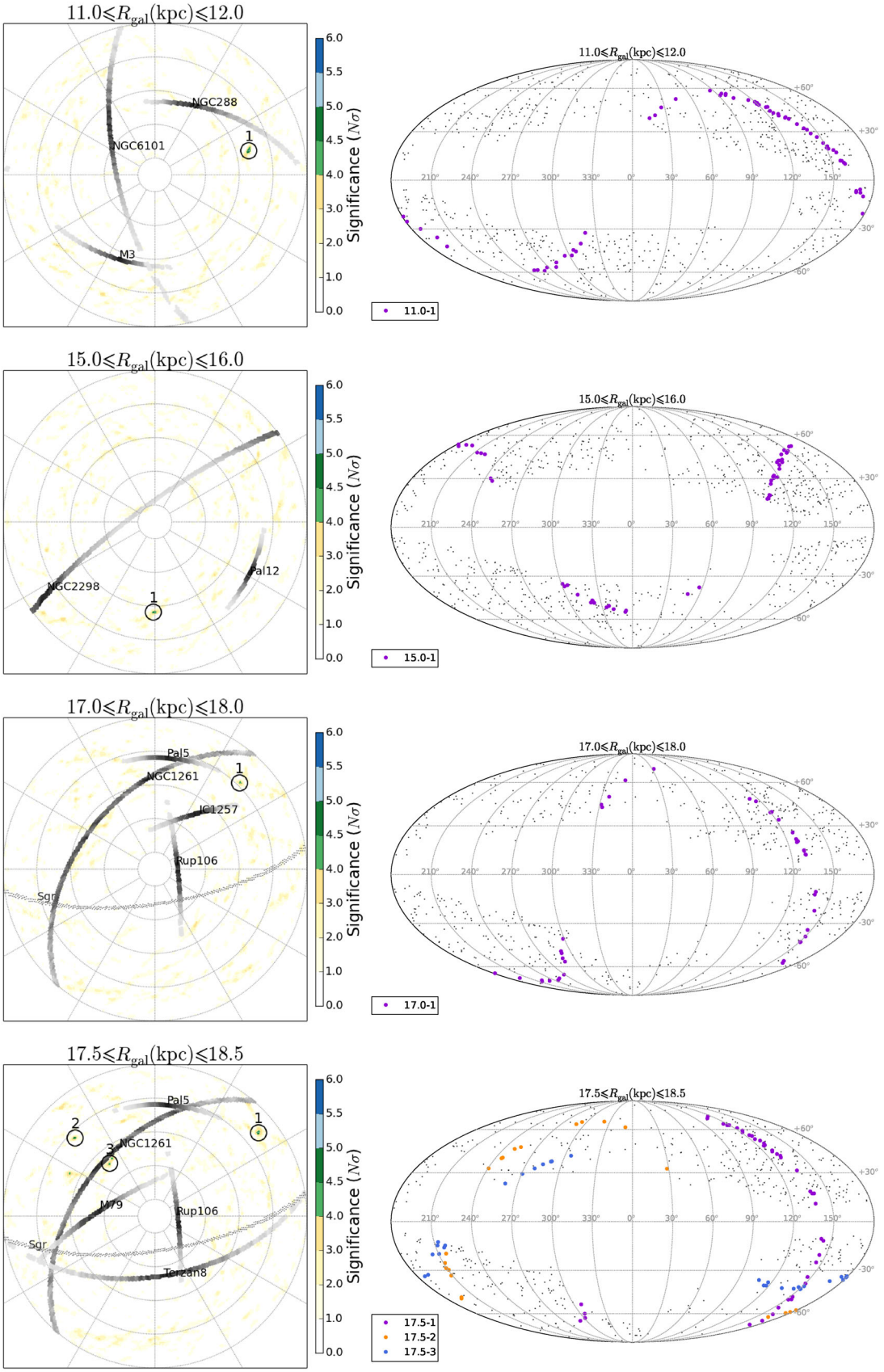

Figure 1 – *continued*

Downloaded from https://academic.oup.com/mnras/article-abstract/474/3/4112/4628071
by University College London user
on 06 March 2018

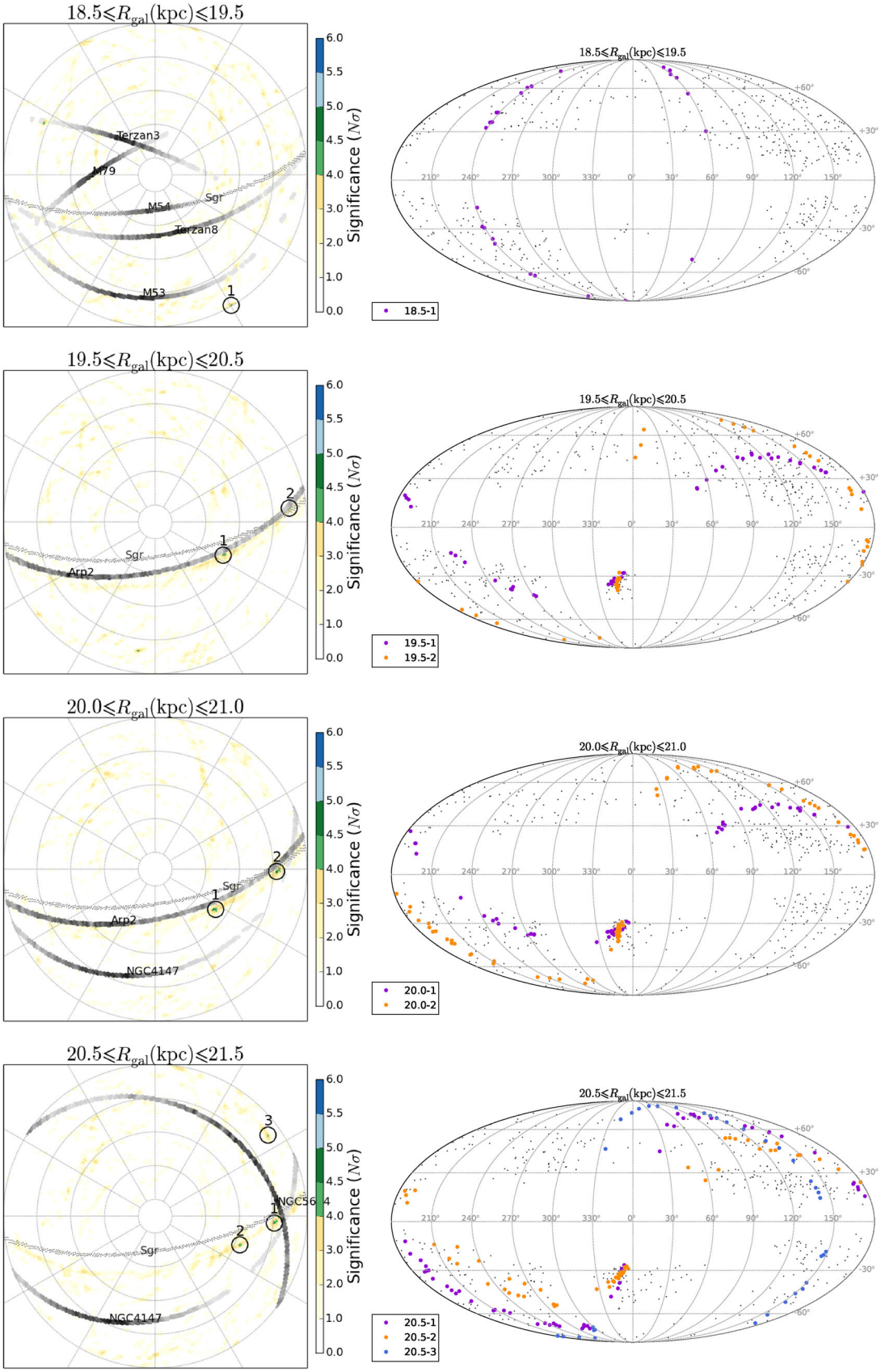

Figure 1 – *continued*

Downloaded from https://academic.oup.com/mnras/article-abstract/474/3/4112/4628071
by University College London user
on 06 March 2018

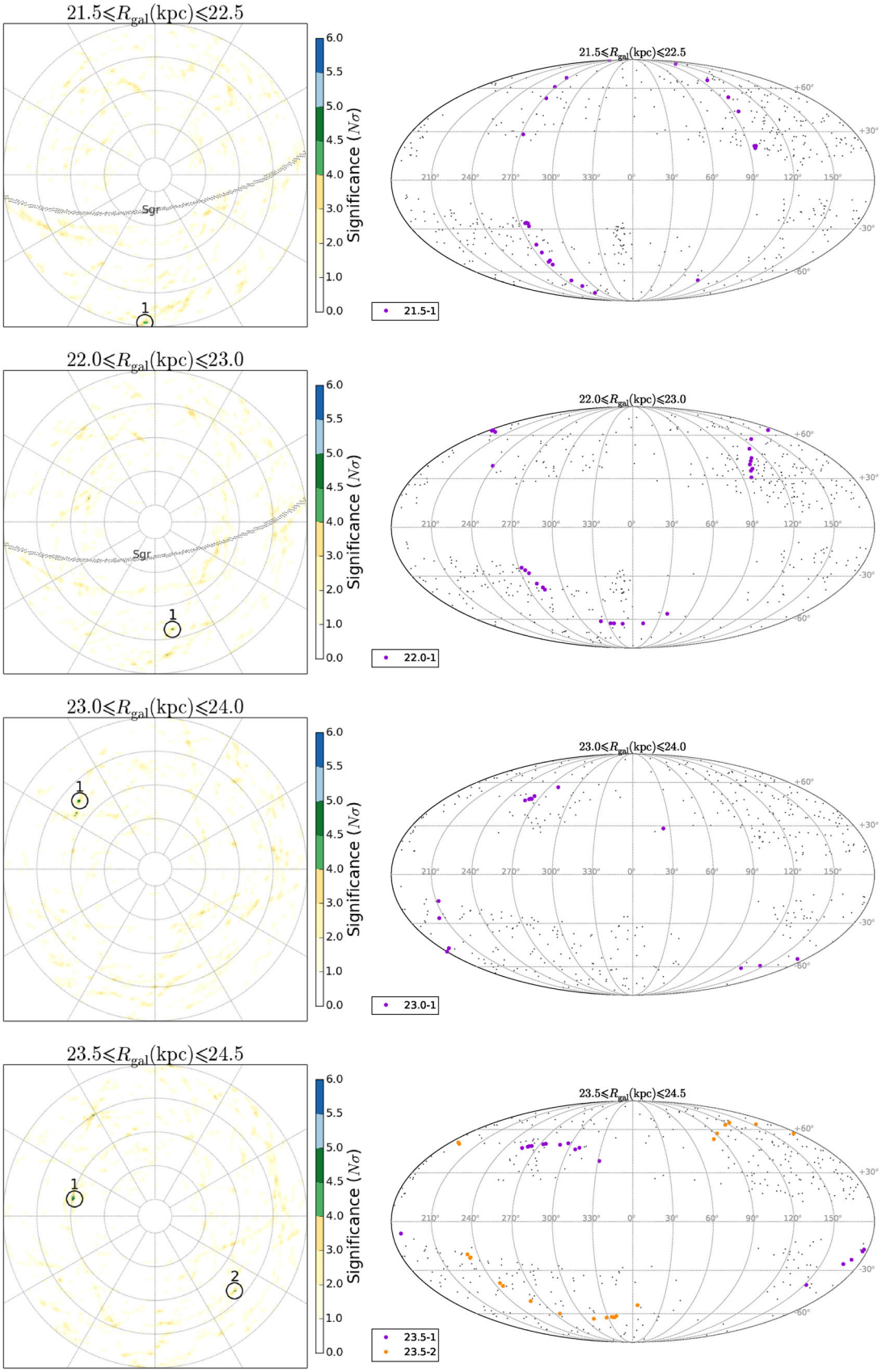

Figure 1 – *continued*

Downloaded from https://academic.oup.com/mnras/article-abstract/474/3/4112/4628071
by University College London user
on 06 March 2018

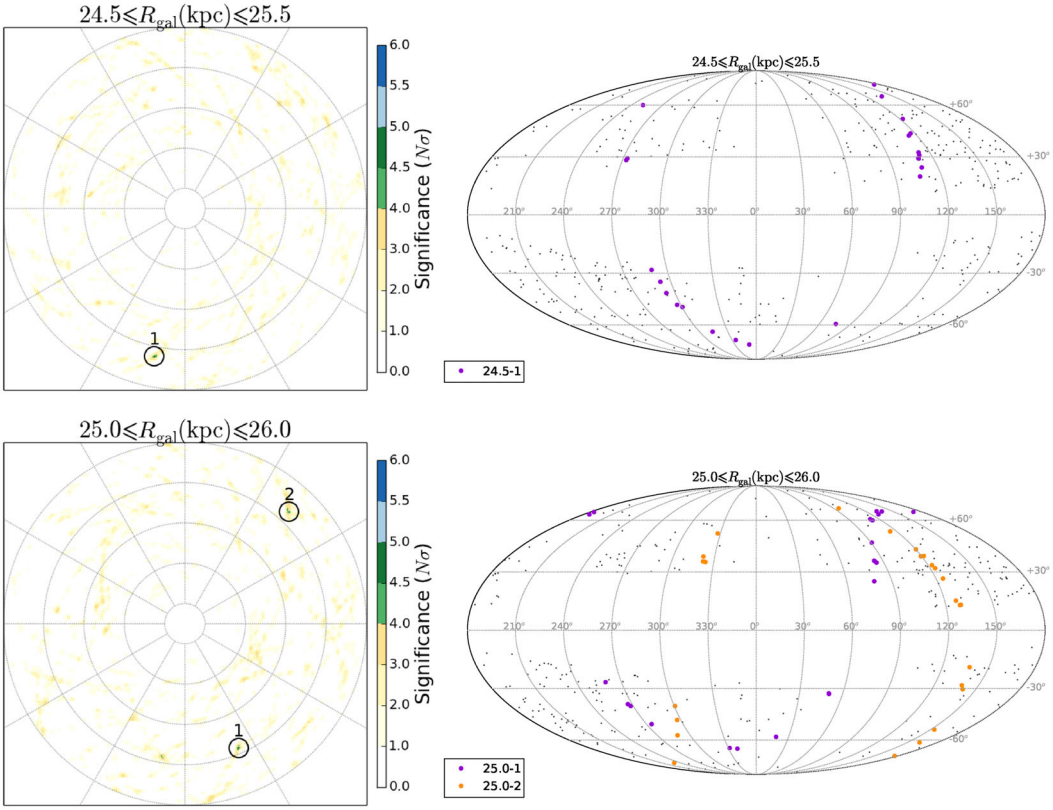

Figure 1 – *continued*

perturbed realization of the RRLS catalogue and 100 bootstrap realizations of this perturbed catalogue to analyse the detection significance as described above. The perturbed catalogue was produced by adding a random step to the equatorial coordinates of each RRLS. The steps were drawn at random from a Gaussian distribution with a standard deviation of 3°, a value chosen to be higher than the width of our *GC3* great-circle cells (2°) to ensure the stars have a non-negligible probability of being perturbed out of their great-circle cell. Repeating the procedure used for the bootstrap analysis, we compute the mean bootstrap significance for the 100 bootstrap realizations of the perturbed catalogue.

In the perturbed catalogue, any real stream within our selected tolerance should have been erased by the random perturbation, so if the bootstrap significance threshold chosen above is appropriate, no detections with a larger significance should be found in the perturbed catalogue. The artefact test results show that no detections have bootstrap significance above 4σ in the high-confidence candidates radial bins, which confirms these are not likely to be artefacts. For the tentative candidates, we mark as artefacts those with a mean bootstrap significance lower than the maximum bootstrap significance of any detections found in the corresponding radial bin in the perturbed catalogue. These are thus reported as *possible artefacts*.[5]

In some cases, e.g. 17.5-1 and 19.5-1, there are multiple detections of the same candidate, due to the 0.5 kpc overlap in our R_{gal} bins. When the pole detections in adjacent radial bins coincide within $\lesssim 5°$, we report that with the highest mean bootstrap significance as the main one, and the rest as *repeated detections*.

Finally, we report detections 19.5-2, 20.0-2, and 20.5-1 as unambiguous detections of the Sagittarius stream (Sgr). These detection's poles coincide within ∼4° with the galactocentric pole (93.°8, +13.°5) reported by Majewski et al. (2003).[6]

4.2 Candidate PCMs and sky distribution

Fig. 1 shows the *GC3* + *nGC3* PCMs in the distance bins where significant (>4σ) peak detections were found.

The left-hand panels ofFig. 1 show the unsharp-masked *GC3* + *nGC3* PCMs in an equidistant north-polar azimuthal projection, with a colour scale proportional to the detection significance expressed in $N\sigma$ units (see Section 3.2). Detected peaks are marked with a circle and labelled in each distance bin with an integer number. The Galactocentric distance bin is indicated at the top of each PCM. Each stream candidate is given a unique ID constructed as the integer label shown in Fig. 1 and the lower limit of the distance bin in which the detection was made (e.g. stream candidates 04.5-1 and 04.5-2 are shown in the top panel of Fig. 1). This ID is used to identify each stream candidate throughout this paper. The right-hand panels of Fig. 1 show the distributions of RRLSs in

[5] In further experiments with perturbed catalogues, we estimate that for bins with $R_{gal} < 20$ kpc no detections with mean bootstrap significance >3σ are expected; while for $R_{gal} > 20$ kpc, we find on average one per R_{gal} bin with mean bootstrap significance above 3σ and none at >4σ.

[6] Majewski et al. (2003) reports the antipodal pole (273.°8, −13.°5), since it coincides with the direction of Sgr's angular momentum. Nevertheless, antipodal poles are equivalent, since both define the same plane under the *xGC3* criteria.

Downloaded from https://academic.oup.com/mnras/article-abstract/474/3/4112/4628071
by University College London user
on 06 March 2018

Table 2. Properties of the stream candidates detected in *GC3 +nGC3* PCMs.

ID	$N_{ab}^{\rm all}$	Purity	$N_{ab}^{\rm exp}$	Oo. fractions			Oosterhoff		M_V	M_V	L_V (P84)	Comment
				I	Int	II	Type	Prob.	Mode	$(-\Delta, +\Delta)$	$(\times 10^5 L_\odot)$	
						High-confidence candidates						
11.0-1	40	0.48	19	0.68	0.17	0.15	...	0.13	−7.5	(−1.51, 1.50)	<8.3	Corvus
20.0-1	32	0.53	17	0.84	0.09	0.06	I	0.05	−7.3	(−1.46, 1.47)	<6.7	Arp2/PS1-C
						Tentative candidates						
04.5-1	23	0.56	13	0.61	0.26	0.13	...	0.06	−6.7	(−1.35, 1.32)	<3.3	
08.0-1	34	0.54	18	0.76	0.06	0.18	...	0.07	−7.4	(−1.47, 1.50)	<6.7	
08.0-2	27	0.53	14	0.85	0.11	0.04	..	0.06	−6.9	(−1.38, 1.37)	<5.0	
09.0-1	42	0.51	22	0.76	0.14	0.10	...	0.07	−7.8	(−1.55, 1.54)	<10.0	
15.0-1	42	0.49	21	0.81	0.10	0.10	I	0.05	−7.7	(−1.53, 1.54)	<10.0	
17.0-1	36	0.47	17	0.75	0.19	0.06	...	0.07	−7.3	(−1.46, 1.47)	<6.7	not-Pal5
17.5-2	23	0.61	14	0.61	0.26	0.13	...	0.06	−6.9	(−1.38, 1.37)	<5.0	Hermus?
17.5-3	18	0.57	10	0.78	0.11	0.11	...	0.10	−6.2	(−1.18, 1.16)	<1.7	NGC1261?
22.0-1	25	0.54	13	0.88	0.04	0.08	I	0.05	−6.7	(−1.35, 1.32)	<3.3	
23.5-1	13	0.68	9	0.85	0.15	0.00	...	0.10	−6.0	(−1.20, 1.00)	<1.7	Hyllus?
23.5-2	22	0.56	12	0.86	0.14	0.00	...	0.06	−6.6	(−1.26, 1.30)	<3.3	
24.5-1	21	0.56	12	0.81	0.14	0.05	...	0.08	−6.6	(−1.26, 1.30)	<3.3	

Table 3. RRLSs associated with each of the stream candidates. (This table is published in its entirety as Supporting Information with the electronic version of the article. A portion is shown here for guidance regarding its form and content).

ID	CSS-SSS-ID	RAJ2000 (°)	DEJ2000 (°)	Rhel (kpc)	Rgal (kpc)	Period (d)	AmpV (mag)	FeH (dex)	flg	pmRA (mas yr^{-1})	pmDE (masyr^{-1})	HSOY-ID
04.5-1	J165107.7-185500	252.78216	−18.91671	12.09	4.56	0.60154	0.64	−1.34	0	−8.1 ± 2.2	−6.3 ± 2.2	4.8426375499386829E18
04.5-1	J203208.8-251433	308.03653	−25.24252	6.01	5.18	0.57042	0.78	−1.38	0	1.8 ± 2.1	−0.5 ± 2.1	5.0354848055937546E18
04.5-1	J204034.3-251227	310.14282	−25.20737	6.00	5.37	0.54851	0.77	−0.96	0	−1.6 ± 2.1	−5.0 ± 2.1	5.0362798660131287E18
04.5-1	J204750.0-271645	311.95815	−27.27923	6.11	5.47	0.66466	0.46	−1.19	0	1.3 ± 2.7	−7.4 ± 2.7	5.0313484201172142E18
04.5-1	J202002.4-292359	305.00997	−29.39977	6.08	4.80	0.50794	1.12	−1.16	0	2.8 ± 2.1	−7.4 ± 2.1	5.014405122247722E18

the current $R_{\rm gal}$ bin, in galactocentric spherical coordinates (ϕ, θ)[7] The stars associated with each of the peaks marked as detected in the corresponding PCM are plotted with different colours, as shown in each panel's legend.

The left-hand panels of Fig. 1 also show the expected *nGC3* signature for all known GCs and dwarf galaxies present in each distance bin, calculated using positions and distances from Harris (1996) and proper motions from Balbinot & Gieles (2017) for GCs, and using all data from McConnachie (2012) for dwarf galaxies. The grey-scale represents the signature expected within 3σ of each cluster's proper motion errors, with the darkest parts corresponding to the highest probability areas. Clusters (or galaxies) produce a signature along a great circle in the PCM, the length of which is inversely proportional to the proper motion errors: good proper motion data constrain the orbital plane well and produce a localized peak, while bad or no proper motion data do not, and so, produce a peak that stretches along a great circle.

These plots allow us to see very quickly which of our stream candidates might be associated with a known GC or dwarf galaxy. The pole detection of candidate 07.0–2 lies right on top of the signature expected from GC Pal11 on a very high probability region. The pole detection of candidate 17.5-3 lies just off NGC1261's great-circle PCM signature and that of 20.0-1 lies along the great-circle signature due to Arp 2. The remaining candidates do not seem to be associated with any known GCs.

[7] In this reference system, the Galactic Disc is located at $\theta = 0°$ and $\phi = 0°$ points *away* from the Sun.

4.3 Candidate RRLS properties

The information related to or inferred from the RRLS in each candidate is summarized in Table 2, shown only for the high confidence and tentative candidates. The list of RRLSs associated with each candidate is given in Table 3.

Table 2 summarizes $N_{\rm RR}^{\rm all}$ the total number of RRLSs associated with each pole detection, the expected purity of each detection, and $N_{\rm RR}^{\rm exp}$ the expected number of RRLSs that would truly belong to the stream candidate, i.e. excluding contaminants. The expected purity is the fraction of stars expected to actually belong to a stream in each detection, after accounting for the contribution of background contaminants, estimated by integrating the pole counts in the smoothed PCM. The fractions of RRLSs of Oosterhoff type I (OoI), Int (OoInt), and II (OoII) are also reported. Stars were classified as OoI, OoInt, and OoII if $\Delta\log P \geq -0.005$, $-0.005 \leq \Delta\log P < -0.04$, and $\Delta\log P \leq -0.04$, respectively, with $\Delta\log P = -0.14V_{\rm amp} - 0.12 - \log P$, where $V_{\rm amp}$ and P are the light curve V-band amplitude and period, following Kunder & Chaboyer (2009) and Clement & Shelton (1999).

To report an 'expected' Oosterhoff type for each candidate we cannot simply look at the relative fractions of stars of each Oosterhoff type, as this will always be dominated by the more abundant OoI stars. Nevertheless, we can use our knowledge of the typical fractions expected for each Oosterhoff type from

Downloaded from https://academic.oup.com/mnras/article-abstract/474/3/4112/4628071
by University College London user
on 06 March 2018

the full CSS+SSS catalogue, which are, respectively, 71 per cent, 14 per cent, and 15 per cent for OoI, OoInt, and OoII RRLSs. We use these fractions, and the total number of RRLSs observed in each candidate $N_{\rm RR}^{\rm all}$, to compute the expected number of stars of each Oosterhoff type and compare these with the actual observed number of RRLSs of each Oosterhoff type. We report as the expected Oosterhoff type that for which the observed number gives the smallest Poisson probability, when this probability is smaller than 0.05. The expected Oosterhoff type and Poisson probability are reported in Table 2. Note that, although the CSS catalogue reports spectroscopic and photometric metallicities (Drake et al. 2013b; Torrealba et al. 2015), we chose not to report a mean metallicity for the candidate streams as this will be dominated by the metallicity of 'normal' halo contaminant stars. Lacking kinematical information, these contaminant RRLSs cannot be distinguished from those that belong to the identified streams, leading to an erroneous metallicity estimate.

The absolute magnitude and total luminosity of the stream candidates, inferred from $N_{\rm RR}^{\rm exp}$, the expected number of RRLSs in each stream, are also reported along with their respective 1σ confidence intervals. The absolute magnitude M_V was estimated using Bayesian Inference and the well-known linear relationship between the absolute magnitude and the (log) number of RRLSs in a stellar population (Suntzeff, Kinman & Kraft 1991; Vivas & Zinn 2006; Mateu et al. 2009). This inference thus corresponds to the absolute magnitude of a system given an observed number of RR*ab* stars, N_{ab}, so it will correspond to the stream's absolute magnitude in most cases; however, if the candidate contains the majority of satellite progenitor stars, this estimate reflects the total M_V of the progenitor plus the stream.

We write the posterior probability density $P(M_V|\log N_{ab})$ as the product of a Gaussian likelihood $L = P(\log N_{ab}|M_V) = \exp(\log N_{ab} - \log N_{ab}^T(M_V))^2/(2\sigma_N^2)$, which assumes a (constant) Gaussian uncertainty in the M_V–$\log N_{ab}$ relationship; and a power-law prior $P(M_V) = 10^{0.1(M_V+5.)}$, given by the luminosity function of MW satellite galaxies obtained by Koposov et al. (2008). We express the M_V–$\log N_{ab}$ relationship as $\log N_{ab} = aM_V + b$, with $a = -0.2402$ and $b = -0.6167$, and assume a standard deviation $\sigma_N = 0.328$ about this relationship. These values were estimated from a least squares fit using data from a compilation of MW classical and ultra-faint dwarf galaxies from Harris (1996), Catelan (2009) and Baker & Willman (2015).[8] The posterior probability density for the luminosity is expressed in terms of that for the absolute magnitude as $P(L_V|\log N_{ab}) = P(M_V(L_V)|\log N_{ab})/L_V$. In Table 2, we report the posterior mode and 1σ confidence intervals for M_V and L_V.

5 COMPARISON WITH KNOWN STREAMS AND HALO SUBSTRUCTURE

5.1 MW streams library and PYTHON package

Grillmair & Carlin (2016) have made a recent compilation to summarize basic average properties of known, well-established streams and clouds in the MW (their tables 4.1 and 4.2). The data they provide in their table 4.1 to illustrate the extent of each stream, as the authors point out, refer only to the coordinate range occupied by each stream in the celestial sphere. Although useful as a first approximation, and reasonably well suited to describe the extent of diffuse cloud-like structures, more specific footprint data are warranted for streams in order to make a fair comparison of the literature to any newly identified substructure.

With this motivation in mind, we have built the PYTHON Package GALSTREAMS, publicly available at https://github.com/cmateu/galstreams. The package contains an MW Streams Library with standardized information about known Galactic streams and clouds and providing a series of utility classes and methods to define, manipulate, and plot the footprint data of all streams registered in the library; with flexible ways to define a stream, making the library easy to expand. The MW Streams Library is based on the Grillmair & Carlin (2016) review and expanded to include new streams published up to 2017 June. Table 4 summarizes the streams and clouds included in the library by default.

The main object classes in GALSTREAMS are as follows: the MWSTREAMS object handles the entire library as a whole, with each stream/cloud being represented as a FOOTPRINT object, which handles the set of coordinates that represent a given stream.

The FOOTPRINT object represents each stream's celestial footprint as a collection of points, i.e. a set of sky coordinate arrays. So for each stream the FOOTPRINT object holds as attributes, the coordinates in all pre-defined systems: equatorial, heliocentric galactic, spherical Galactocentric, and Cartesian heliocentric and Galactocentric coordinates. The main feature of the FOOTPRINT class is that it allows instantiating or creating any stream in one of four different ways, defined in the GCUTILS library, by giving one of the following:

(i) Start and end point coordinates
(ii) Orbital pole coordinates and, optionally, the stream's centre, length, and width
(iii) A coordinate range (more suitable for clouds)
(iv) A list of individual coordinates

For any of this four options, the input coordinates can be provided in the equatorial or (heliocentric) Galactic reference frames and heliocentric distance information is optional. Using the available information, the FOOTPRINT class computes all needed (and possible) coordinate transformations in order for the FOOTPRINT object to have the coordinates in all pre-defined systems mentioned above.

It is this overall flexibility that allows the library to be easily extended as new streams are reported or recovered from the literature. It also allows the user to quickly create a FOOTPRINT object for a stream of interest, without needing to include it in the library.

The GALSTREAMS GitHub repository[9] includes a detailed description of the GALSTREAMS package capabilities, so we refer the reader there for more details. Also, for non-PYTHON users, individual files are provided containing the footprints of all streams and clouds in the library at this URL.[10] In the remainder of this section, Figs 2–4 will showcase the footprints for the streams and clouds stored in the MW Streams Library, summarized in Table 4. Currently the library includes spatial information, i.e. celestial coordinates and distances where available, but it can be easily extended to include further information such as radial velocities, proper motions, metallicity and elemental abundances.

5.2 High-confidence candidates

Fig. 2 shows the sky distribution of the high-confidence candidates relative to known streams and other halo substructure in the

[8] Note that this relationship is valid for $M_V > -5$ and $N_{ab} \geq 3$.

[9] https://github.com/cmateu/galstreams

[10] https://github.com/cmateu/galstreams/tree/master/footprints

Downloaded from https://academic.oup.com/mnras/article-abstract/474/3/4112/4628071
by University College London user
on 06 March 2018

Table 4. Streams and clouds in the MW Streams Library included in the GALSTREAMS PYTHON package.

Name	Reference	Name	Reference	Name	Reference
Alpheus	Grillmair et al. (2013)	Monoceros	Grillmair & Carlin (2016)	PS1-D	Bernard et al. (2016)
Acheron	Grillmair (2009)	Molonglo	Grillmair (2017a)	PS1-E	Bernard et al. (2016)
ACS	Grillmair (2006)	Murrumbidgee	Grillmair (2017a)	Sangarius	Grillmair (2017b)
ATLAS	Koposov et al. (2014)	NGC5466	Grillmair (2006)	Scamander	Grillmair (2017b)
Cetus	Newberg et al. (2009)	Ophiucus	Bernard et al. (2014)	Styx	Grillmair (2009)
Cocytos	Grillmair (2009)	Orphan	Newberg et al. (2010)	Tri-And	Grillmair & Carlin (2016)
GD-1	Grillmair (2006)	Orinoco	Grillmair (2017a)	Tri-And2	Grillmair & Carlin (2016)
EBS	Grillmair & Carlin (2016)	Pal 5	Grillmair (2006)	Tri/Pis	Bonaca et al. (2012)
Eridanus	Myeong et al. (2017)	Pal 15	Myeong et al. (2017)	VOD/VSS	Grillmair & Carlin (2016)
Eri/Phe	Li et al. (2016)	PAndAS	Grillmair & Carlin (2016)	WG1	Agnello (2017)
Hermus	Grillmair (2014)	Phoenix	Balbinot et al. (2016b)	WG2	Agnello (2017)
Her-Aq	Grillmair & Carlin (2016)	PiscesOv	Grillmair & Carlin (2016)	WG3	Agnello (2017)
Hyllus	Grillmair (2014)	PS1-A	Bernard et al. (2016)	WG4	Agnello (2017)
Kwando	Grillmair (2017a)	PS1-B	Bernard et al. (2016)		
Lethe	Grillmair (2009)	PS1-C	Bernard et al. (2016)		

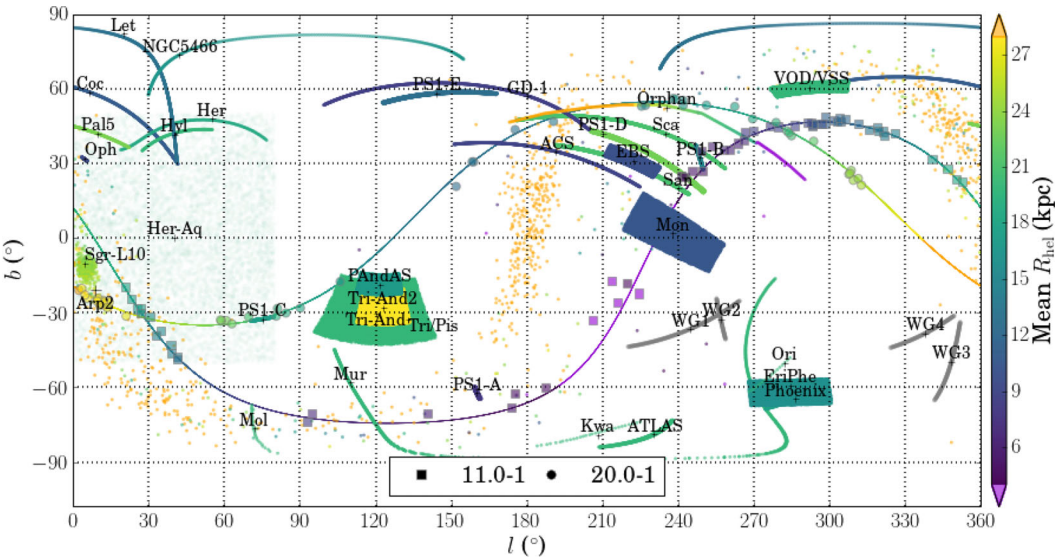

Figure 2. Galactic (heliocentric) latitude versus longitude map for the high-confidence candidates. The RRLSs belonging to each candidate are indicated with different symbols, as shown in the legend and the colour scale is proportional to the heliocentric distance. Each of our candidate's great-circle is shown with a solid line passing through the RRLSs. The streams and clouds from the MW Streams Library that have any overlap in the figure's heliocentric distance range are shown with coloured dots and labelled in the plot. The corresponding references are summarized in Table 4.

MW Streams Library, in a (heliocentric) latitude versus longitude plot, with a colour scale proportional to the heliocentric distance $R_{\rm hel}$. The symbols represent the RRLSs associated with each candidate: squares for candidate 11.0-1 and circles for candidate 20.0-1. The solid line that goes along each candidate's RRLS is the great circle defined by the candidate's pole given in Table 1. Note that, because this plot is heliocentric, each candidate spans a range of several kpcs in $R_{\rm hel}$, as the colour scale shows even though, by construction of our search strategy, it's *Galactocentric* radial extent is <1 kpc.

Torrealba et al. (2015) has also searched for overdensities in the southern SSS part of the Catalina survey, included in our Catalina+HSOY RRLS catalogue (Section 2). In their table 3, they report the central equatorial coordinates and extent of the 26 overdensities they identified, shown also in their fig. 14. In Fig. 3, we compare the location of our high-confidence candidates to their 12 reported overdensities with a significance $\geq 3\sigma$, in an RA-DEC map similar to Fig. 2, with a colour scale proportional to heliocentric distance. This comparison is approximate because we use the data of Torrealba et al.'s table 3 to represent their overdensities, as rectangles in RA-DEC and their fig. 14 show them to be more general polygonal areas. Nevertheless, even with this simplification, the figure still serves our purpose to check for approximate spatial coincidences between our candidates and their overdensities.

5.2.1 *Candidate 11.0-1 – Corvus stream*

Candidate 11.0-1 is the one with the highest bootstrap significance. The PCM in Fig. 1 shows it is not related to any known GC or dwarf galaxy.

The densest part of this candidate, which causes the peak in the PCM, is located at $240^\circ \lesssim l \lesssim 330^\circ$. In particular, as Fig. 2 shows, the region around $240^\circ \lesssim l \lesssim 270^\circ$ is quite crowded with known substructures: the PS1-B, PS1-D, Sangarius, Scamander, and Orphan streams cross that region, but are most likely independent of our stream candidate as they cross the 11.0-1 great circle almost orthogonally. They are also much more distant than our candidate:

Downloaded from https://academic.oup.com/mnras/article-abstract/474/3/4112/4628071
by University College London user
on 06 March 2018

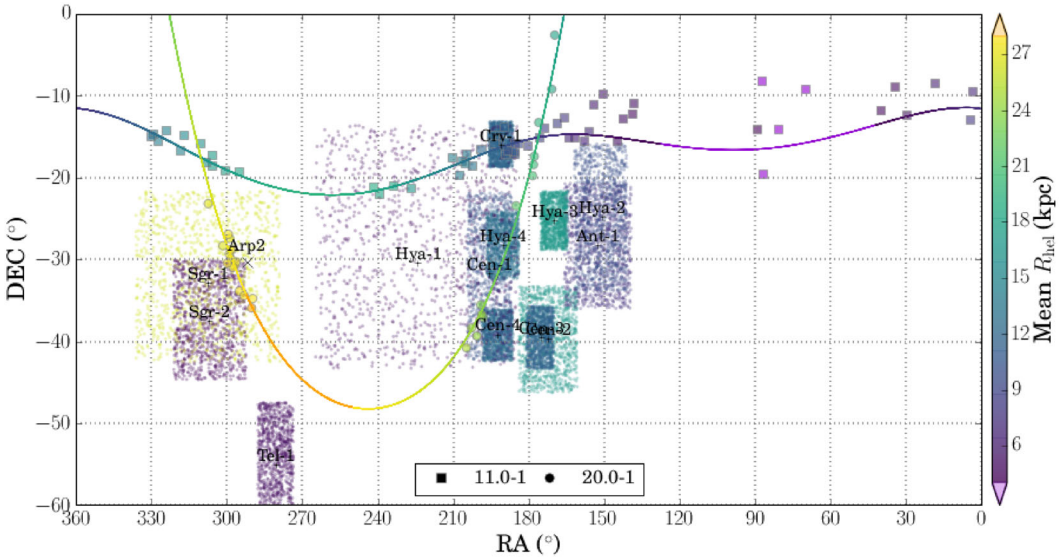

Figure 3. Equatorial coordinates map for the high-confidence candidates and significant overdensities found by Torrealba et al. (2015) in the SSS survey. The RRLSs belonging to each candidate are indicated with the same symbols as in Fig. 2, as shown in the legend. The colour scale is proportional to the heliocentric distance. Each of our candidate's great circle is shown with a solid line passing through the RRLSs.

in this region, the 11.0-1 RRLSs are located at $R_{\rm hel} \sim 7$ kpc, while these streams are at least twice as distant, with PS1-B being the closest at $\sim 14.5^{+3.7}_{-3.0}$ kpc (Bernard et al. 2016) and the rest having distances >18 kpc. The southern part of the 11.0-1 candidate at $l \lesssim 40^\circ$ lies close to the edge of the Sgr tail, but in this area our candidate's RRLSs lie at $R_{\rm hel} \sim 18$ kpc and the Sgr tail is much more distant (>28 kpc), so it is not a likely contaminant.

Out of the total 40 RR*ab* stars associated with this detection, we expect ∼19 RR*ab* to be real stream stars, given that its purity is estimated at 0.48. The fraction of RRLSs of different Oosterhoff types are fairly consistent with those of the typical halo field (see Section 4.3), so no information can be inferred at this point about the possible Oosterhoff type of this candidate.

In Fig. 3, we compare in an RA–DEC plot the spatial distribution of our high-confidence candidates and SSS overdensities from Torrealba et al. (2015), where we have also included Crv 1 (2.99σ), although it is just below the 3σ threshold. This overdensity lies right along our 11.0-1 candidate and at the same distance (∼12 kpc) as our candidate's RRLS in that region. Nevertheless, after removing the RRLS in the Crv 1 region the 11.0-1 detection is still recovered at the same pole, with a 4.2σ significance. This confirms 11.0-1 is an independent detection and traces a structure larger than the reported extent of Crv 1, although without kinematics it is not possible to estimate its real extent. The central coordinates $(l, b) = (300.^\circ4, +46.^\circ84)$ reported for Crv 1 by Torrealba et al. (2015) are also fairly close to the densest part of our candidate, $(l_\bigcirc, b_\bigcirc) = (288.^\circ98, +46.^\circ21)$, at an angular distance <7°, supporting that the RRLS in that area are the best follow-up candidates to characterize the stream and to look for a potential progenitor.

Duffau et al. (2016) and Navarrete et al. (2016) suggest Crv 1 might be a possible southern extension of the Virgo Stellar Stream. However, the orbital plane shown in Fig. 2 for 11.0-1 with respect to the VSS[11] does not seem to support this. *Gaia* proper motions combined with radial velocities from the spectroscopic survey being conducted by these authors will be decisive to clarify whether the two are related.

In summary, the properties of the 11.0-1 detection suggest the Crv 1 overdensity is more extended than originally reported and is a stream-like overdensity. We propose naming it the *Corvus stream* to keep Torrealba et al.'s designation and following the usual convention for streams.

5.2.2 *Candidate 20.0-1 – Arp2/PS1-C*

Fig. 1 shows our multiple detections of this candidate (19.5-2, 20.0-1, and 20.5-2) lie right on top of the Arp 2 GC's signature in the PCM, suggesting a possible association between the two. At first this is just a hint. The proper motion errors for Arp 2 are quite high, which is why its PCM signature shows up as a full great circle, as it is only constrained by the cluster's position. Nevertheless, in this candidate, the largest concentration of RRLS *is* found very near the centre of Arp 2, at $(l_\bigcirc, b_\bigcirc) = (7.^\circ8, -23.^\circ9)$ (see Table 1), as Fig. 2 also illustrates. The fact that there are two more detections of this candidate (19.5-1 and 20.5-2) with very similar poles differing only by ∼5°, reinforces that it is unlikely this candidate would be a random excess due to outlying Arp 2 RRLS, in which case it would be more natural to expect pole count excesses at random poles along the Arp 2 great circle. Also, since in our pre-processing of the RRLS catalogue all the stars inside the tidal radius of each GC were removed (see Section 2.1), the RRLS excess is likely due to tails and not to the GC's bound core itself.

It also seems unlikely that this candidate's detection is due to the Sgr stream. The Law & Majewski (2010) Sgr spherical model (shown in the figures) predicts the tails in this region to be much more distant (>30 kpc) and if the peak detected in the PCM were just a spurious peak induced by left-over RRLS just outside the Sgr core, there is no reason why the detection should coincide so well with the Arp 2 great circle in the PCM *and do so over three radial distance bins*. In the event that Sgr RRLSs were causing a random excess, it is unlikely that a significant PCM peak would be detected almost in the same position over three radial bins (two of which, 19.5 and 20.5, have no overlapping stars and, so, are entirely

[11] Virgo Stellar Stream.

Downloaded from https://academic.oup.com/mnras/article-abstract/474/3/4112/4628071
by University College London user
on 06 March 2018

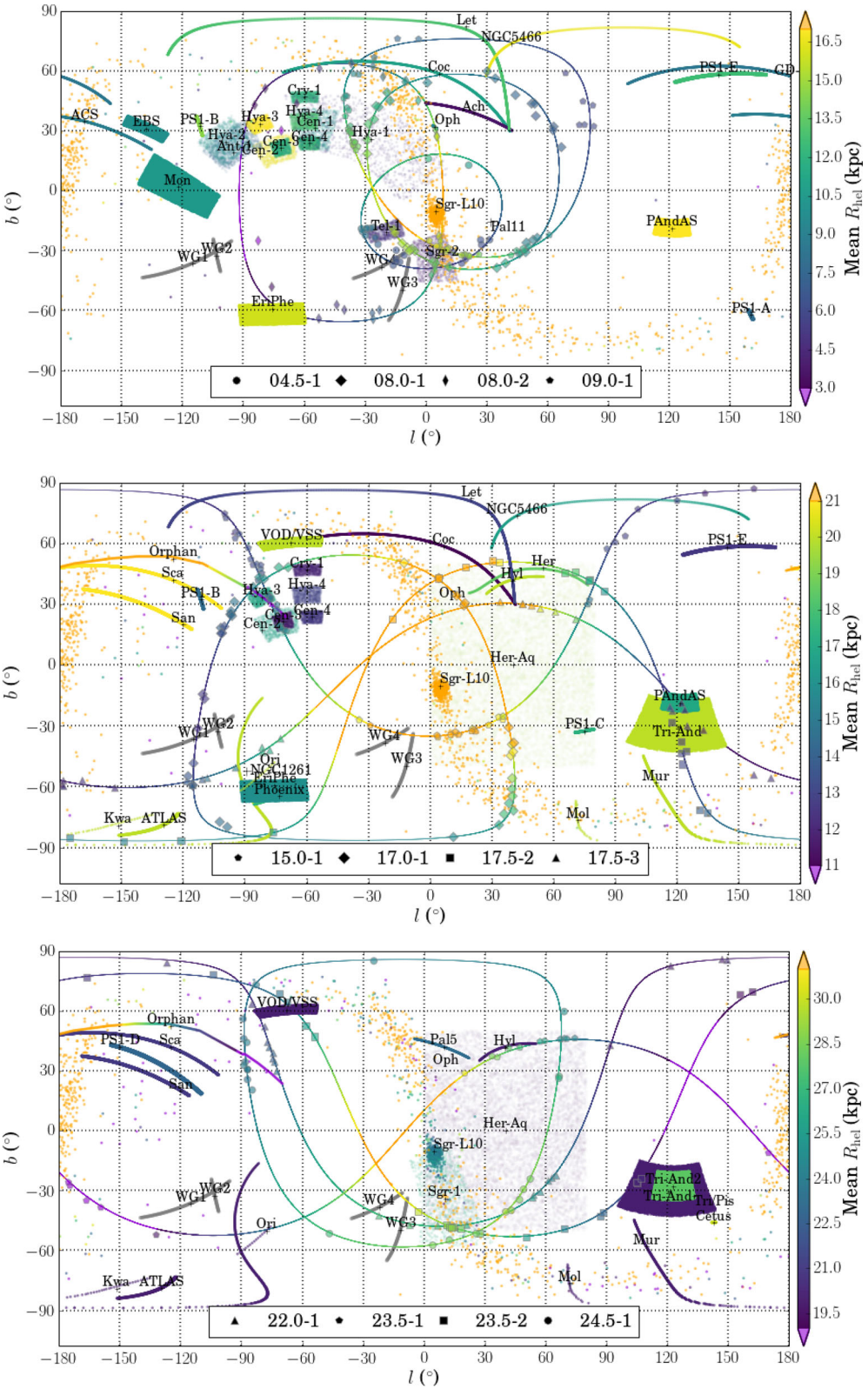

Figure 4. Galactic (heliocentric) latitude versus longitude map for the tentative candidates. The three panels show candidates ordered by their Galactocentric distance: 4–10 kpc *top*, 15–21 kpc *middle,* and 21–26 kpc *bottom*. As in Fig. 2, the colour scale is proportional to the heliocentric distance and the RRLSs belonging to each candidate are indicated with different symbols, as shown in the legend. Each of our candidate's great circle is shown with a solid line passing through the RRLSs. The streams and clouds from the MW Streams Library that have any overlap in each plot's heliocentric distance range are shown with coloured dots and labelled in the plot. The corresponding references are summarized in Table 4.

Downloaded from https://academic.oup.com/mnras/article-abstract/474/3/4112/4628071
by University College London user
on 06 March 2018

independent), differing by only a few degrees and always along the Arp 2 great circle.

Fig. 2 shows this candidate might also be associated with the PS1-C stream (Bernard et al. 2016). The PS1-C stream coincides exactly with the 20.0-1 great circle in the plane of the sky and the distance is very similar: Bernard et al. (2016) reports a heliocentric distance of $17.4^{+3.5}_{-3.6}$ kpc for PS1-C and the RRLSs in this area have a distance around ∼19 kpc, which are in agreement within the errors. We also removed the RRLS around the PS1-C stream (17 RRLS with $19.5 < R_{\rm gal}$(kpc) < 21.5) and found the peak is still detected in the PCM at the same pole, with only a slightly decreased significance (4.8σ compared to the initial 5.2σ). This confirms that 20.0-1 is an independent detection since the PCM excess is not dominated by PS1-C RRLS, but rather by the RRLS closer to Arp 2.

Bernard et al. (2016) suggest PS1-C might be related to the Balbinot 1 stellar cluster (Balbinot et al. 2013), which lies very near ($(l, b) = (75\overset{\circ}{.}2, -32\overset{\circ}{.}6)$) the reported centre for PS1-C (shown with a cross in Fig. 2). However, this association does not seem likely at first since, according to Balbinot et al.'s distance estimate ($R_{\rm hel} = 31.9$ kpc), the cluster is located at $R_{\rm gal} = 31.2$ kpc, much more distant than our stream candidate.

The Orphan stream also partly coincides with the 20.0-1 candidate in the *l*–*b* plane at $l \in [180^\circ - 210^\circ]$, but it is much more distant lying at $\gtrsim 30$ kpc compared to a mean distance ∼14 kpc of the candidate's RRLSs in this area. This implies the Orphan stream is not the cause of the 20.0-1 PCM excess, but it is interesting to note that the two orbital planes – and, therefore, their poles – are relatively similar, which suggests the possibility that they might be related.

The RRLS content of 20.0-1 has a fraction of 0.84 Oo type I stars, compared to the expectation of 0.71, which marginally favours an Oosterhoff type I classification, as does detection 20.5-1, with a very similar Oo I fraction. However, detection 19.5-1 more clearly favours an Oo Int type, with an observed fraction of 0.27 Oosterhoff Intermediate stars, almost twice the expected fraction of 0.14. According to Catelan (2009), Arp 2 is one of the few existing Oo Intermediate GCs (only 4 out of their 41 clusters are classified as Oo Int) and it is considered to be associated with the Sgr dwarf galaxy, also Oosterhoff Intermediate. Although we have argued that the 20.0-1 candidate's PCM detection is unlikely to be due to Sgr entirely, some Sgr contamination is inevitably expected due to our current lack of kinematic information. Therefore, the evidence regarding the Oo type of this candidate is still inconclusive, but worth being analysed in a future study.

Fig. 3 shows the 20.0-1 candidate also overlaps with Sgr 1, a large overdensity spanning over 80 deg^2 according to the RA/DEC. extent reported by Torrealba et al., which they claim 'is almost certainly a part of the Sgr stream'. We have two arguments to believe 20.0-1 is a distinct substructure within the Sgr 1 overdensity: the angular scale of Sgr 1 is much larger, with a typical width of ∼20° compared to $1\overset{\circ}{.}8$ for 20.0-1; and we have argued above why, despite the inevitable contamination from Sgr, this candidate is more likely to be caused by a tidal tail from GC Arp 2.

Thus, we take the 20.0-1 candidate as a *new detection* that appears to be a thin stream *within* the candidate Sgr 1 overdensity, and it is potentially related to the Arp 2 cluster and even possibly the PS1-C stream.

The differences and partial coincidences with the Torrealba et al. (2015) results are to be expected since our RRLS catalogue contains the SSS catalogue in its entirety, but our search methods are very different. Torrealba et al. searched for overdensities by comparing the local estimated density of RRLSs in SSS to the density expected from a halo-only model, a method more suited to search for wide extended or cloud-like overdensities; our method, on the other hand, is specifically designed to search for planar substructure.

5.3 Tentative candidates

Fig. 4 shows the spatial distribution of our tentative candidates in an *l*–*b* map, similarly to Fig. 2, with a colour scale proportional to heliocentric distance. The three panels span different heliocentric distance ranges chosen appropriately to show case the candidates in three galactocentric distance ranges: $R_{\rm gal} \in [4, 10]$ in the *top* panel; $R_{\rm gal} \in [15, 18]$ in the *middle* panel; and $R_{\rm gal} \in [22, 25]$ in the *bottom* panel. As in Fig. 2, each candidate's great circle is shown with a solid line. Known MW streams and Torrealba et al. (2015) SSS overdensities are also shown.

In what follows we will discuss the tentative candidates that may be associated with known streams or GCs.

5.3.1 Candidate 17.0-1 – not Pal 5

The PCM in Fig. 1 shows that candidate 17.0-1's peak lies ∼40° away from the Pal 5 orbital pole in the same great circle, well outside the signature expected for Pal 5 accounting for 3σ proper motion errors, which suggests the two are probably unrelated. This is also illustrated in the middle panel of Fig. 4, where candidate 17.0-1 is shown with thick diamond symbols (◇). 17.0-1's great circle passes close to Pal 5 at a very different angle, and also the densest concentration of RRLSs along the great circle is found at $(l_{\bigcirc}, b_{\bigcirc}) = (261.3, 19.7)$, quite far from Pal 5, over 90° away in longitude. Therefore, this candidate is not likely to be associated with Pal 5. On the other hand, the main overdensity in the 17.0-1 candidate is relatively close, and at the same distance $R_{\rm hel} \sim 17$ kpc, as the Hya 3 overdensity from Torrealba et al. (2015), suggesting a possible connection between the two.

5.3.2 Candidate 17.5-2 – Hermus?

Candidate 17.5-2 is not related to any known GC according to the PCM in Fig. 1. As the middle panel of Fig. 4 shows (square symbols), it passes close to the Hermus stream (Grillmair 2014) in the sky. The densest part of 17.5-2 is right at the end of the Hermus stream as reported by Grillmair (2014) at $(l_{\bigcirc}, b_{\bigcirc}) = (75\overset{\circ}{.}3, 42\overset{\circ}{.}8)$ (see Table 1) and at the same distance ∼18 kpc.

Grillmair & Carlin (2016) cite a possible metallicity for this stream around [Fe/H] ∼ − 2.3 and mention that efforts are in progress to associate RRLSs or other tracers, such as blue horizontal branch stars, to this stream. Ours would then be the first identification of RRLS potentially associated with the Hermus stream, which will have to be confirmed with kinematic data. This will also help us confirm which of this candidate's RRLSs in the rest of the great circle are a true coherent overdensity and whether what we're seeing could be a bifurcation of the Hermus stream.

5.3.3 Candidate 17.5-3 – NGC1261?

The PCM of Fig. 1 shows candidate 17.5-3's pole coincides with GC NGC1261's great circle, which hints at a possible association between the two. This is just a hint at first because the proper motions for this cluster have very large uncertainties (> 100 per cent in RA)

Downloaded from https://academic.oup.com/mnras/article-abstract/474/3/4112/4628071
by University College London user
on 06 March 2018

and do not constrain the orbital plane well, which is why the PCM signature is a full great circle rather than a less extended feature (see Section 3.1).

There is little evidence regarding the RRLS content of this candidate either. According to Catelan (2009), this is a Young-Halo GC, Oosterhoff type I. Its metallicity is [Fe/H] = −1.35, and it has 13 known RR*ab* stars. This is consistent with the 78 per cent of OoI RRLSs in this candidate, but this fraction is also fairly close to the mean expected one from field RRLSs. Hence, a possible association of 17.5-3 with NGC1261 remains tentative.

5.3.4 Candidate 23.5-1 – Hyllus?

Candidate 23.5-1 is shown with pentagon symbols in the bottom panel of Fig. 4, which shows it passes very close in the sky to the Hyllus stream (Grillmair 2014). Grillmair & Carlin (2016) cite a *mean* heliocentric distance of ∼20 kpc for Hyllus (which we use in the figure), but Grillmair (2014) report a distant gradient, estimating distances of 18.5 ± 3 and 23 ± 3 kpc for the northern and southern ends, respectively (in equatorial coordinates). The 23.5-1 RRLS in its vicinity span heliocentric distances from 28 to 25 kpc at the $l \sim 30^\circ$ and $l \sim 60^\circ$ ends that correspond to Hyllus's (equatorial) northern and southern ends, respectively. At the southern end, the distances are well in agreement with Grillmair's estimate of 23 ± 3 kpc, within the errors, with our RRLS having a mean distance of 25 kpc at $l \in [60^\circ, 80^\circ]$. This is also where the densest part of the 23.5-1 candidate is located, $(l_\bigcirc, b_\bigcirc) = (66^\circ, +45^\circ)$ (see Table 1).

Note also that the bootstrap significance for this candidate is 3.9σ, so it was not classified as high-confidence, but it is just below the selected threshold of 4σ; thus, even though classified as tentative, this seems to be a fairly good detection. Therefore, it seems likely that the 23.5-1 candidate is the first independent detection of the Hyllus stream made with RRLSs and that we may have identified a southern extension of the stream going from $(l, b) \sim (56^\circ, 44^\circ)$ to $(76^\circ, 47^\circ)$.

6 COMPARISON WITH PREDICTIONS AND KNOWN GC TIDAL TAILS

Three GCs have tidal tails detected in SDSS or Pan-STARRS, according to Balbinot & Gieles (2017): Pal 5 (Odenkirchen et al. 2003), NGC 5897 (Price-Whelan private communication cited by Balbinot & Gieles 2017), and NGC 5466 (Belokurov et al. 2006a; Grillmair & Johnson 2006; Fellhauer et al. 2007). The first two have a very scarce population of RR*ab* stars. The Pal 5 cluster itself has five known RRLSs, all of type *c* (Clement et al. 2001; Sawyer Hogg 1973); Vivas et al. (2001) and Vivas & Zinn (2006) have identified 2 type *ab* RRLSs (out of a total of 6) in the cluster tails; and NGC 5897 has 3 type *ab* out of a total of 11 RRLSs (Clement et al. 2001; Clement 2010). Again, it is natural that with such a low number of type *ab* RRLSs, these clusters' tails could not be recovered by our analysis. NGC 5466, on the other hand, has 13 known RR*ab* stars (Catelan 2009) at $R_{\rm gal} = 16.9$ kpc, well within the distance range probed by our study, and Grillmair & Dionatos (2006) reports a 1°.4 width for this cluster's tidal tail. We do not find any pole count excess in the PCMs at NGC 5466's radial distance. However, as we have cautioned, we do not expect our stream candidate sample to be complete due to the lack of kinematic data.

Balbinot & Gieles (2017) present a recent study of the formation of tidal tails in GCs, in which they take into account the collisional dynamical effects, such as mass segregation, produced by internal evolution of the cluster. They find that low-mass stars are preferentially ejected at the early stages of a cluster's disruption and higher mass stars are only ejected as the cluster comes close to complete dissolution. This effect naturally produces an observational bias, making tidal tails of fully dissolved GCs more easily observable than those of clusters that still retain a bound core. Balbinot & Gieles offer this as an explanation of why tidal tails have been found only around very few GCs and predict that new surveys will preferentially find 'orphan' or progenitor-less GC streams. This prediction supports our findings that only 2 out of our 14 candidate streams could (possibly) be associated with known GCs. These are 17.5-3 and 20.0-1 that might be related to NGC 1261 and Arp 2, respectively (see Section 5.3.3).

Balbinot & Gieles (2017) also offer general predictions for which known GCs are most likely to have detectable tidal tails, based on the cluster's position and velocity data. Their candidates Pal 1 (15.9 kpc), Pal 7 (3.6 kpc), and M56 (NGC 6779, 9.5 kpc) are in the low-latitude exclusion zone $|b| \leq 20^\circ$ of the CSS+SSS surveys, while Whiting 1 (49.5 kpc) is outside the distance range probed in our analysis ($R_{\rm gal} < 25$ kpc). This leaves us with their GC candidates AM4 ($R_{\rm gal} = 24.8$ kpc), NGC 288 (11.4 kpc), and M92 (NGC 6341, 9.5 kpc), the latter two being their best candidates in terms of optimal detectability.

For a proper comparison with our results, we must also consider each cluster's stellar population and known RRLS content, since our survey is based on RRLS of type *ab* alone, which are not present in some GCs and are scarce in several. According to Catelan (2009), NGC 288 is a classical second-parameter cluster, with a very blue horizontal branch and only one reported RR*ab* star (and one RR*c*) according to Arellano Ferro et al. (2013). AM 4 is an extremely faint cluster ($M_V = -1.8$, Carraro 2009) with almost no discernible red giant branch (Hamren et al. 2013). It harbours no variable stars according to Clement et al. (2001), Clement (2010), and references therein. Therefore, neither NGC 288's nor AM 4's tails would be detectable with an RRLS sample.

Thus, out of the candidates proposed by Balbinot & Gieles (2017), only M92 could be detected with our RRLS sample. This cluster has 11 known RR*ab* stars (Catelan 2009) and is well within the distance range of our study ($R_{\rm gal} = 9.5$ kpc). Although its tidal tails, if present, should be detectable with our current sample, in our PCMs we do not find any evidence of a pole count excess that could be associated with this cluster. There is one candidate in the same distance bin as M92 (9.0-1). However, Fig. 1 shows that its pole is tens of degrees away from the pole-count signature expected for this cluster. We stress, however, that given our lack of kinematic information (required to reduce background contamination), we cannot rule out the possibility that M92 has tidal tails.

7 CONCLUSIONS

We have applied the GC3 stream-finding method to RRLSs in the Catalina survey that is sensitive to nearby streams over the Galactocentric distance range $4 < D/\text{kpc} < 26$. Our key results are as follows:

(i) We detect two high-confidence ($>4\sigma$) new RRLS stream candidates:
– *Candidate 11.0-1* includes the recently discovered Crv 1 RRLS overdensity (Torrealba et al. 2015), but is a larger structure. We call this the 'Corvus stream'.
– *Candidate 20.0-1* appears to trace tidal tails around the Arp 2 GC that might be connected to the PS1-C stream (Bernard et al. 2016).

Downloaded from https://academic.oup.com/mnras/article-abstract/474/3/4112/4628071
by University College London user
on 06 March 2018

Proper motions and/or radial velocities are needed to test this scenario. This candidate also spatially coincides with the Sgr 1 overdensity found by Torrealba et al. (2015), but is much thinner (∼1°.8) than Sgr-1 (∼20°, see Section 5.2.2). We call this the 'Arp2/PS1-C stream'.

(ii) We detect of 12 tentative RRLS stream candidates ($>3.5\sigma$). Out of these, three are of particular interest: candidates 17.5-2 and 23.5-1 could be possible extensions of the Hermus and Hyllus streams, respectively, and candidate 17.5-3 could be associated with GC NGC1261.

(iii) Our high-confidence stream candidates are expected to host ∼17-19 RR*ab* , accounting for MW halo contaminants. This number of RRLS implies an absolute magnitude $M_V \sim -7.4 \pm 1.5$ for the underlying population, which translates into an upper bound of $\sim 7 \times 10^5 L_\odot$ for the total luminosity. For the low-confidence candidates, the number of expected RR*ab* stars ranges from 9 to ∼20 and inferred absolute magnitudes from $M_V \sim -6$ to -7.8. These are summarized in Table 2.

(iv) We do not find any candidate stream around M92, the only cluster out of the tidal tail candidates proposed by Balbinot & Gieles (2017) that could be detectable with our RRLS sample. However, due to background contamination from the MW stellar halo, we are not able to rule out tidal tails around M92. For this, kinematic data are required.

(v) Of our 14 stream candidates, only two – 17.5-3 (NGC 1261) and 20.0-1 (Arp2) – are potentially associated with known GCs. This supports the idea that, due to mass segregation, tidal tails around GCs only become detectable close to full dissolution, leading to a high fraction of orphan GC streams (Balbinot & Gieles 2017).

(vi) Our detections are likely a lower bound on the total number of dissolving GCs in the inner Galaxy. Many GCs have few RRLSs, while only the brightest streams are visible over the Galactic RRLS background. A more complete census will be possible with the inclusion of velocity data.

We make all of our data public and provide the PYTHON Package GALSTREAMS,[12] which stores footprint information for all currently known Galactic streams and clouds, with utility classes and methods to define, manipulate, and plot these data. This library, where data are publicly available, is extensible so that more detailed information on each stream can be added.. We will keep the data base updated with new streams and structures as they are found.

ACKNOWLEDGEMENTS

CM is indebted to Luis Aguilar, Cesca Figueras, Mercè Romero-Gómez, and Bárbara Pichardo for their unwavering support. CM, DK, JIR also thanks Luis Aguilar and Bárbara Pichardo for organizing the Mexico Gaia Meeting 2016, where this work began, and in which they strived to provide an enjoyable environment that would foster open and relaxed discussions and collaborations between the participants. CM acknowledges support from the ICC University of Barcelona Maria de Maeztu visiting academic grants. CM is grateful for the hospitality of the University of Surrey, MSSL, and the organizers of the IV Gaia Challenge Workshop, where part of this research was carried out, and warmly thanks Mark Gieles for an interesting discussion about the formation of tails in GCs. JIR would like to acknowledge support from STFC consolidated grant (CG) ST/M000990/1 and the MERAC foundation. DK acknowledges support from STFC CG (ST/N000811/1).

[12] https://github.com/cmateu/galstreams.

REFERENCES

Abedi H., Mateu C., Aguilar L. A., Figueras F., Romero-Gómez M., 2014, MNRAS, 442, 3627
Agnello A., 2017, MNRAS, 471, 2013
Altmann M., Roeser S., Demleitner M., Bastian U., Schilbach E., 2017, A&A, 600, L4
Anderhalden D., Schneider A., Macciò A. V., Diemand J., Bertone G., 2013, JCAP, 3, 014
Arellano Ferro A., Bramich D. M., Giridhar S., Figuera Jaimes R., Kains N., Kuppuswamy K., 2013, Acta Astron., 63, 429
Baker M., Willman B., 2015, AJ, 150, 160
Balbinot E., Gieles M., 2017, preprint (arXiv:1702.02543)
Balbinot E. et al., 2013, ApJ, 767, 101
Balbinot E. et al., 2016a, ApJ, 820, 58
Balbinot E. et al., 2016b, ApJ, 820, 58
Baur J., Palanque-Delabrouille N., Yèche C., Magneville C., Viel M., 2016, J. Cosmol. Astropart. Phys., 8, 12
Belokurov V., Evans N. W., Irwin M. J., Hewett P. C., Wilkinson M. I., 2006a, ApJ, 637, L29
Belokurov V. et al., 2006b, ApJ, 642, L137
Bernard E. J. et al., 2014, MNRAS, 443, L84
Bernard E. J. et al., 2016, MNRAS, 463, 1759
Berry D. S., 2015, Astron. Comput., 10, 22
Bonaca A., Geha M., Kallivayalil N., 2012, ApJ, 760, L6
Brodie J. P., Strader J., 2006, ARA&A, 44, 193
Bullock J. S., Boylan-Kolchin M., 2017, ARA&A, 55, 343
Bullock J. S., Kravtsov A. V., Weinberg D. H., 2001, ApJ, 548, 33
Cacciari C., Corwin T. M., Carney B. W., 2005, AJ, 129, 267
Carlberg R. G., 2012, ApJ, 748, 20
Carraro G., 2009, AJ, 137, 3809
Catelan M., 2009, Astrophys. Space Sci., 320, 261
Clement C. M., 2010, in Sterken C., Samus N., Szabados L., eds, Variable Stars, the Galactic halo and Galaxy Formation. Sternberg Astronomical Institute of Moscow University, Russia
Clement C. M., Shelton I., 1999, ApJ, 515, L85
Clement C. M. et al., 2001, AJ, 122, 2587
D'Onghia E., Springel V., Hernquist L., Keres D., 2010, ApJ, 709, 1138
Diemand J., Kuhlen M., Madau P., 2007, ApJ, 667, 859
Drake A. J. et al., 2013a, ApJ, 763, 32
Drake A. J. et al., 2013b, ApJ, 765, 154
Duffau S. et al., 2016, CoKon, 105, 199
Erkal D., Koposov S. E., Belokurov V., 2017, MNRAS, 470, 60
Eyre A., Binney J., 2009, MNRAS, 400, 548
Fellhauer M., Evans N. W., Belokurov V., Wilkinson M. I., Gilmore G., 2007, MNRAS, 380, 749
Gaia Collaboration et al., 2016a, A&A, 595, A1
Gaia Collaboration et al., 2016b, A&A, 595, A2
Grillmair C. J., Dionatos O., 2006, ApJ, 643, L17
Grillmair C. J., 2009, ApJ, 693, 1118
Grillmair C. J., 2014, ApJ, 790, L10
Grillmair C. J., 2017a, ApJ, 847, 119
Grillmair C. J., 2017b, ApJ, 834, 98
Grillmair C. J., Carlin J. L., 2016, in Newberg H. J., Carlin J. L., eds, Astrophysics and Space Science Library Vol. 420, Tidal Streams in the Local Group and Beyond. Springer Int. Publ., Switzerland, p. 87
Grillmair C. J., Johnson R., 2006, ApJ, 639, L17
Grillmair C. J., Cutri R., Masci F. J., Conrow T., Sesar B., Eisenhardt P. R. M., Wright E. L., 2013, ApJ, 769, L23
Hamren K. M., Smith G. H., Guhathakurta P., Dolphin A. E., Weisz D. R., Rajan A., Grillmair C. J., 2013, AJ, 146, 116
Harris W. E., 1996, AJ, 112, 1487
Ibata R., Irwin M., Lewis G. F., Stolte A., 2001a, ApJ, 547, L133
Ibata R. A., Lewis G. F., Irwin M. J., Cambrésy L., 2001b, MNRAS, 332, 921
Ibata R. A., Lewis G. F., Irwin M. J., Quinn T., 2002, MNRAS, 332, 915
Johnston K. V., Hernquist L., Bolte M., 1996, ApJ, 465, 278

Downloaded from https://academic.oup.com/mnras/article-abstract/474/3/4112/4628071
by University College London user
on 06 March 2018

Johnston K. V., Spergel D. N., Haydn C., 2002, ApJ, 570, 656
Johnston K. V., Law D. R., Majewski S. R., 2005, ApJ, 619, 800
Jurcsik J., Kovacs G., 1996, A&A, 312, 111
Klypin A., Kravtsov A. V., Valenzuela O., Prada F., 1999, ApJ, 522, 82
Koposov S. et al., 2008, ApJ, 686, 279
Koposov S. E., Rix H.-W., Hogg D. W., 2010, ApJ, 712, 260
Koposov S. E., Irwin M., Belokurov V., Gonzalez-Solares E., Yoldas A. K., Lewis J., Metcalfe N., Shanks T, 2014, MNRAS, 442, L85
Kovacs G., Kupi G., 2007, A&A, 462, 1007
Kunder A., Chaboyer B., 2009, AJ, 138, 1284
Kunder A., Chaboyer B., Layden A., 2010, AJ, 139, 415
Küpper A. H. W., Balbinot E., Bonaca A., Johnston K. V., Hogg D. W., Kroupa P., Santiago B. X., 2015, ApJ, 803, 80
Law D. R., Majewski S. R., 2010, ApJ, 714, 229
Li T. S. et al., 2016, ApJ, 817, 135
Lux H., Read J. I., Lake G., 2010, MNRAS, 406, 2312
Lux H., Read J. I., Lake G., Johnston K. V., 2013, MNRAS, 436, 2386
Lynden-Bell D., Lynden-Bell R. M., 1995, MNRAS, 275, 429
Majewski S. R., Skrutskie M. F., Weinberg M. D., Ostheimer J. C., 2003, ApJ, 599, 1082
Martin J. C., Morrison H. L., 1998, AJ, 116, 1724
Mateu C., 2014, Astrophysics Source Code Library, record ascl:1411.011
Mateu C., Vivas A. K., Zinn R., Miller L. R., Abad C., 2009, AJ, 137, 4412
Mateu C., Bruzual G., Aguilar L., Brown A. G. A., Valenzuela O., Carigi L., Velázquez H., Hernández F., 2011, MNRAS, 415, 214
Mateu C., Vivas A. K., Downes J. J., Briceño C., Zinn R., Cruz-Diaz G., 2012, MNRAS, 427, 3374
Mateu C., Cooper A. P., Font A. S., Aguilar L., Frenk C., Cole S., Wang W., McCarthy I. G., 2017, MNRAS, 469, 721
Mateu C., 2017, Astrophysics Source Code Library. Available at: https://ascl.net/code/v/1827
McConnachie A. W., 2012, AJ, 144, 4
Moore B., Ghigna S., Governato F., Lake G., Quinn T., Stadel J., Tozzi P., 1999, ApJ, 524, L19
Moore B., Diemand J., Madau P., Zemp M., Stadel J., 2006, MNRAS, 368, 563
Myeong G. C., Jerjen H., Mackey D., Da Costa G. S., 2017, ApJ, 840, L25
Navarrete C. et al., 2016, IAU, 11, 338
Navin C. A., Martell S. L., Zucker D. B., 2016, ApJ, 829, 123
Neeley J. R. et al., 2017, ApJ, 841, 84
Newberg H. J., Yanny B., Willett B. A., 2009, ApJ, 700, L61
Newberg H. J., Willett B. A., Yanny B., Xu Y., 2010, ApJ, 711, 32
Newton O., Cautun M., Jenkins A., Frenk C. S., Helly J., 2017, preprint (arXiv:1708.04247)
Odenkirchen M. et al., 2003, AJ, 126, 2385
Peñarrubia J., Benson A. J., Walker M. G., Gilmore G., McConnachie A. W., Mayer L., 2010, MNRAS, 406, 1290
Planck Collaboration XVI, 2014, A&A, 571, A16
Read J. I., Moore B., 2005, MNRAS, 361, 971
Read J. I., Wilkinson M. I., Evans N. W., Gilmore G., Kleyna J. T., 2006, MNRAS, 367, 387
Read J. I., Agertz O., Collins M. L. M., 2016, MNRAS, 459, 2573
Read J. I., Iorio G., Agertz O., Fraternali F., 2017, MNRAS, 467, 2019
Roeser S., Demleitner M., Schilbach E., 2010, AJ, 139, 2440
Sawala T. et al., 2016, MNRAS, 457, 1931
Sawyer Hogg H., 1973, Publications of the David Dunlap Observatory Univ., Toronto, 3, 1
Sesar B., Fouesneau M., Price-Whelan A. M., Bailer-Jones C. A. L., Gould A., Rix H.-W., 2017, ApJ, 838, 107
Smoot G. F. et al., 1992, ApJ, 396, L1
Springel V., Frenk C. S., White S. D. M., 2006, Nature, 440, 1137
Suntzeff N. B., Kinman T. D., Kraft R. P., 1991, ApJ, 367, 528
Thomas G. F., Famaey B., Ibata R., Lüghausen F., Kroupa P., 2017, A&A, 603, A65
Torrealba G. et al., 2015, MNRAS, 446, 2251
VandenBerg D. A., Denissenkov P. A., Catelan M., 2016, ApJ, 827, 2
Varghese A., Ibata R., Lewis G. F., 2011, MNRAS, 417, 198
Vivas A. K., Zinn R., 2006, AJ, 132, 714
Vivas A. K. et al., 2001, ApJ, 554, L33
White S. D. M., Rees M. J., 1978, MNRAS, 183, 341

SUPPORTING INFORMATION

Supplementary data are available at *MNRAS* online.

Please note: Oxford University Press is not responsible for the content or functionality of any supporting materials supplied by the authors. Any queries (other than missing material) should be directed to the corresponding author for the article.

This paper has been typeset from a TEX/LATEX file prepared by the author.

Downloaded from https://academic.oup.com/mnras/article-abstract/474/3/4112/4628071
by University College London user
on 06 March 2018